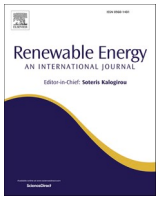
Renewable Energy 254 (2025) 123664



Contents lists available at ScienceDirect

Renewable Energy

journal homepage: www.elsevier.com/locate/renene





# Advanced cooling strategies for highly concentrated PV-T systems: Confined jet impingement, thermoelectric generator integration with channel configurations

Abhishek Gupta [a], Sandesh S. Chougule [b,*], Sandip K. Saha [a]

[a] Department of Mechanical Engineering, Indian Institute of Technology Bombay, Mumbai, 400076, India
[b] Clean Energy Processes (CEP) Laboratory, Department of Chemical Engineering, Imperial College London, London, SW72AZ, United Kingdom

ARTICLE INFO

*Keywords:*
Confined jet impingement
Efficiency
Highly concentrated photovoltaic cell
Hybrid cooling
Stress
Thermoelectric generator

ABSTRACT

The present study focuses on the cooling of a highly concentrated photovoltaic thermal (HCPV-T) system with a hybrid cooling consisting of confined jet impingement cooling and a thermoelectric generator in the presence of a spectral splitter to keep the cell temperature within the permissible limit of 110 °C. The thermoelectric generator module is used to generate extra electrical energy using the waste heat of the HCPV-T system. Channel design involves a central inlet and four outlets at the heat sink corners. The effect of ten distinct channel configurations by varying the fin angle, fin width, and pitch is studied in the present study. The maximum cell temperature is within the permissible limit with channel configurations C4, C5, C7, C8, and C10. The overall performance of the HCPV-T system is optimum with the channel configuration C4 with a 45° fin angle, 9 mm pitch, and 2.5 mm fin width. The generated cell electrical power is 1037.3 W with configuration C4, with a minimal pressure drop of 1423 Pa. The temperature distribution across the cell surface is more uniform with configuration C5. The combined electric power generated by the HCPV-T system and TEG module is highest with configurations C5 and C7. However, the performance evaluation criterion and overall exergy efficiency are maximum with configuration C4. The power generation from waste heat will help increase the system's overall efficiency.

## Nomenclature

| | |
|---|---|
| $A$ | Area of solar cell ($m^2$) |
| $V$ | Solar cell volume ($m^3$) |
| $T$ | Temperature (°C) |
| $CR$ | Concentration ratio |
| $q$ | Heat generation ($W/m^3$) |
| $I$ | Direct solar irradiation ($W/m^2$) |
| $I_g$ | Electric current in thermoelectric generator (amp) |
| $G$ | Concentrated solar irradiation ($W/m^2$) |
| $\dot{m}$ | Mass flow rate (kg/min) |
| $k$ | Thermal conductivity (W/m·K) |
| $H$ | Combined thickness of the Cu and Ge layers (m) |
| $P$ | Power (W) |
| $C_p$ | Specific heat (J/kg·K) |
| $Q$ | Energy (W) |
| $E$ | Exergy (W) |
| $\Delta T$ | Temperature difference (°C) |
| $h$ | Convective heat transfer coefficient ($W/m^2 \cdot K$) |
| $\vec{V}$ | Velocity vector (m/s) |

## Greek symbols

| | |
|---|---|
| $\mu$ | Viscosity of water (Pa·s) |
| $\sigma$ | Stefan-Boltzmann constant ($W/m^2 \cdot K^4$) |
| $\alpha$ | Absorptivity |
| $\sigma_b$ | Bending stress (Pa) |
| $\nu$ | Poisson ratio |
| $\rho$ | Water density ($kg/m^3$) |
| $\eta$ | Efficiency (%) |
| $\beta_T$ | Cell temperature coefficient |
| $\sigma_T$ | Thermal stress (Pa) |
| $\alpha_T$ | Thermal expansion coefficient ($K^{-1}$) |
| $\lambda$ | Wavelength (nm) |

## Subscript

| | |
|---|---|
| cell | solar cell |
| a | ambient |
| Cu | Copper |

(*continued on next page*)

* Corresponding author.
*E-mail addresses:* s.chougule@imperial.ac.uk, sandesh_chougule@yahoo.com (S.S. Chougule), sandip.saha@iitb.ac.in (S.K. Saha).

https://doi.org/10.1016/j.renene.2025.123664
Received 24 February 2025; Received in revised form 12 May 2025; Accepted 3 June 2025
Available online 6 June 2025
0960-1481/© 2025 The Author(s). Published by Elsevier Ltd. This is an open access article under the CC BY license (http://creativecommons.org/licenses/by/4.0/).

(*continued*)

| | |
|---|---|
| conv | convection |
| fric | frictional |
| out | outlet |
| Ge | Germanium |
| eff | effective |
| el | electrical |
| f | fluid |
| in | inlet |
| opt | optical |
| Ce | Ceramic |
| m | mean |
| ref | reference |
| rad | radiation |
| th | thermal |
| al | aluminium |
| max | maximum |

Abbreviations

| | |
|---|---|
| CPV | Concentrated photovoltaic |
| CTE | Coefficient of thermal expansion |
| HCPV | Highly concentrated photovoltaic |
| HTC | Heat transfer coefficient |
| HCPV-T | Highly concentrated photovoltaic thermal |
| JI | Jet impingement |
| MOI | Moment of inertia |
| PV | Photovoltaic |
| CJI | Confined jet impingement |
| TEG | Thermoelectric generator |

## 1. Introduction

Solar energy is one of the most significant sources of renewable energy. It has a high potential to meet the energy consumption of the world in the future [1,2]. Photovoltaic (PV) systems are used to obtain electrical energy from solar energy, and solar thermal collectors are used to convert solar energy to thermal energy. Combining solar thermal collectors with PV systems can generate both thermal and electrical energy outputs simultaneously. The conversion efficiency of PV cells can be enhanced by photovoltaic thermal (PV-T) systems. However, in flat-plate PV-T systems, thermal exergy remains relatively low. Consequently, concentrated photovoltaic thermal (CPV-T) systems have been developed as a more effective solution to address these challenges. CPV-T systems are an alternative to replace expensive semiconductor materials with cheaper concentrating systems [3].

The CPV-T systems use lenses or mirrors to concentrate solar radiation onto the cell surface. Concentrated irradiation allows solar cells to generate more electrical energy per unit area. However, the CPV-T system faces many challenges despite these advantages. Only a small fraction of the solar energy is transformed into electrical energy using CPV-T systems. A large portion of the available energy is transformed into heat, which increases the temperature of the PV cell. Gupta et al. [4] reported that the cell temperature could reach 876 °C under a $CR = 800$ suns without any cooling system. Zahhad et al. [5] reported that the $T_{cell}$ could reach 1360 °C under $CR = 1000$ suns without any cooling system. The high cell temperature adversely affects the electrical efficiency of the cell. The conversion efficiency of the cell is reduced by 0.098 % as the $T_{cell}$ increases by 1 °C under CR = 200 suns [6]. The highly concentrated solar irradiation results in problems associated with thermal fatigue and current mismatching. Hence, the CPV-T systems need cooling systems to avoid the problems associated with current mismatching, thermal stress, and temperature non-uniformity.

Passive and active cooling are commonly used cooling methods to keep the CPV temperature within permissible limits. Many cooling techniques, such as jet impingement (JI) [7], liquid immersion cooling, air cooling, phase change materials, heat pipe cooling [8], nanomaterials [9,10], and micro-channel cooling [11], Thermoelectric cooling have been used by various researchers. Several published studies have investigated the concept of changing the spectral response of solar cells to avoid the absorption of waste photons that cannot cause electron-hole pair generation [12,13]. The spectrally selective approach can be used to decrease the cell temperature without any extra energy required, and without moving parts [14]. The other passive cooling methods include phase change material (PCM) cooling, thermoelectric cooling (TEC), and heat pipe cooling. The thermoelectric generators are used to convert waste heat into electrical energy. Chen et al. [15] studied the performance of thermal concentrated solar TEGs, examining three different TEG geometries. The authors reported that for a constant TEG element length, reducing the cross-sectional area leads to an increase in the electrical output of the TEG module. Sabry et al. [16] conducted both experimental and numerical studies on CPV-TEG hybrid systems, assessing the impact of TEG modules with varying sizes and junction counts. They concluded that the proposed CPV-TEG system generates higher net electrical power than a standalone CPV system. The CPV-TEG hybrid system's generated power increased by 7.4 %, 5.8 %, and 3 % for TEG modules measuring 30 × 30 mm, 40 × 40 mm, and 62 × 62 mm, respectively. Kohan et al. [17] developed a 3-D model for a TEG and PV system and evaluated the TEG effect on the performance of the PV system by placing the TEG module on the PV cell backside. The combined TEG and PV system produced more electrical power than a PV system alone; however, the increase in power was marginal. Hence, a cooling system for PV cells is preferable to a hybrid PV and TEG system.

It was observed from the above literature that passive cooling methods are used to cool non-concentrated PV or low-concentrated PV (LCPV) systems. However, the temperature of HCPV-T systems cannot be maintained within the permissible limit by passive cooling methods [18]. Various researchers have investigated the heat transfer characteristics of the JI cooling technique [19,20]. The JI cooling technique can be used to cool densely packed PV cell systems and maintain temperature uniformity [21]. Javidan et al. [22] performed experiments on non-CJI cooling of a PV module measuring 36 × 27.5 cm and found that the $T_{cell}$ reduced to 33.68 °C from 63.95 °C under $I = 1000$ W/m$^2$. Bahaidarah et al. [23] reported temperature uniformity within 1 °C, and the $T_{cell}$ decreased to 36.6 °C with $\dot{m} = 1.5$ L/min under $I = 1000$ W/m$^2$ with non-CJI cooling. Zubeer et al. [24] showed that the LCPV system temperature can be decreased from 64.1 °C to 36.5 °C with non-CJI cooling with a $\dot{m} = 3$ L/min, where the dimensions of the PV module is 1968 mm × 990 mm. Markal et al. [25] found that the $T_{cell}$ was reduced by 61.5 %, and power was improved by 13.2 % by employing 6 nozzles for air jets to cool a PV cell of dimension 157 mm × 145 mm. Amanlou et al. [26] showed that increasing airflow from $8 \times 10^{-3}$ to $16 \times 10^{-3}$ kg/s improved the $\eta_{cell}$ of a 0.8 m × 1 m LCPV cell by 13.5 %. Dong et al. [27] used a T-shaped channel with v = 0.64 m/s to cool a PV cell under CR = 500 and found that the temperature uniformity of 26 °C was maintained. Barrau et al. [28] attained ≈ 2 °C temperature uniformity using a modified hybrid heat sink with microchannels with $1.8 \times 10^{-4}$ m$^3$/s of flow rate and CR = 458. Zahhad et al. [5] found a reduction in $T_{cell}$ from 1360 °C to 65 °C, achieving a 6 °C of temperature uniformity using water at $\dot{m} = 50$ g/min for $CR = 1000$ suns using the CJI cooling technique. However, the channels were not introduced in their study. Gupta et al. [4] studied the effect of a CJI cooling scheme on the performance of the HCPV-T system by introducing channel configurations. The authors proposed five different channel configurations and found that the mini-channel configuration provides maximum cooling with minimal pressure drop and maximum temperature uniformity. The $T_{cell}$ was reduced to 55 °C under $CR = 1000$ with a pressure drop of 163 Pa and maintained a temperature uniformity of 6.3 °C across the PV cell surface. Tang et al. [29] used ultrathin micro pin-fin channels and observed the $T_{cell}$ as 51 °C at $CR = 1000$ at $\dot{m} = 3$ kg/h with circular and square pin-fin designs showing pressure drops of 2.73 kPa and 5.29 kPa, respectively, at $\dot{m} = 1.5$ kg/h. Shohdy et al. [30] found a 20.6 °C temperature uniformity at a $\dot{m} = 200$ g/min by using trimmed fins and microchannels at $CR = 2500$. The summary of the literature review is

shown in Table 1.

It can be inferred from the reviewed studies that passive cooling techniques alone are insufficient to dissipate heat from solar cells in high concentrations for continuous operations. Therefore, active cooling methods are required to be incorporated to cool and maintain the temperature of HCPV-T systems within the safe operational limit. In this context, the jet impingement cooling technique is an effective solution for the thermal management of HCPV-T systems due to its relatively higher heat transfer coefficient. However, most studies are substantially restricted to non-CJI cooling, where multiple nozzles are used to maintain temperature uniformity across the PV cell surface [31]. To avoid using several nozzles due to limited space, the CJI cooling technique can effectively reduce the cell temperature by maintaining the cell temperature uniformity. The published literature shows that a major portion of the available solar energy does not contribute to electrical energy output and is released in the form of heat, thereby increasing the solar PV cell's temperature beyond its operational limits. It is reported that only the photons in the 300–1100 nm wavelength range have very high energy and can cause the electron-hole pair of the solar PV cell to be partially converted into electricity [32]. Hence, a spectral splitter with a high transmissivity for the 300–1100 nm wavelength range can be used along with the CJI cooling technique to improve the electrical output by reducing the operational temperature of the HCPV-T system. Furthermore, the generated waste heat can be converted into electrical energy output using a secondary electricity converter in the form of the TEG modules based on the Seebeck effect. Only a few researchers have studied the effect of hybrid cooling on concentrated HCPV-T system performance, but limited to JI and microchannel cooling [28], TEG and PCM cooling [33], JI and PCM cooling [34], TEG and nano-enhanced channel cooling [35], Heat pipe and PCM cooling [36], and JI and heat pipe cooling [37]. Therefore, the originality of the current study is based on the novel proposed hybrid cooling method for HCPV-T systems, combining a spectral splitter, CJI with channel configurations, and TEG cooling. Mini-channel configurations are employed in this CJI cooling system to achieve the cell temperature within the permissible limits with lower pressure drop and higher exergy efficiency. The TEG module in the current model can generate extra electrical power using the waste heat. A three-dimensional, steady-state model of the HCPV-T system, comprised of a solar PV cell, heat sink with channel configurations, and a TEG module, is developed using the finite volume method (FVM) approach. The effect of various fin angles, fin widths, and pitch on the cell maximum temperature and cell temperature uniformity is analysed. Moreover, the cell electrical and thermal efficiency, exergy efficiency, and generated thermal stress variation in the PV cell are performed for different channel configurations. An optimum channel configuration is proposed by considering the performance evaluation criterion and overall exergy efficiency of the HCPV-T system.

**Table 1**
Summary of the literature review.

| Author | Type of cooling | Remarks |
|---|---|---|
| Chen et al. [15] | TEG cooling | TEG electrical output reduces with a decrease in cross-sectional area for a constant TEG length |
| Sabry et al. [16] | TEG cooling for CPV systems | CPV-TEG hybrid system's generated power increased by 7.4 %, 5.8 %, and 3 % for 30 × 30 mm, 40 × 40 mm, and 62 × 62 mm TEG modules. |
| Kohan et al. [17] | TEG cooling for PV systems | The increase in electrical power from the PV-TEG system is only marginal that from a PV system alone. |
| Javidan et al. [22] | JI cooling for a 36 × 27.5 cm PV module | Tcell reduced to 33.68 °C from 63.95 °C under I = 1000 W/m2 |
| Bahaidarah et al. [23] | JI cooling for a PV system | Tcell decreased to 36.6 °C with $\dot{m}$ = 1.5 L/min under I = 1000 W/m2 with a temperature uniformity of 1 °C |
| Zubeer et al. [24] | JI cooling for an LCPV system | Tcell decreased from 64.1 °C to 36.5 °C with a $\dot{m}$ = 3 L/min |
| Markal et al. [25] | Air jet cooling for PV systems | Tcell was reduced by 61.5 % and power was improved by 13.2 % by employing 6 nozzles. |
| Dong et al. [27] | Microchannel cooling for CPV systems | T-shaped channels were used to cool the CPV system under CR 500 with v = 0.64 m/s. A temperature uniformity of 26 °C was found. |
| Barrau et al. [28] | Modified hybrid heat sink with microchannels | Temperature uniformity of 2 °C was attained for densely packed cells under CR = 458 with 1.8 × 10-4 $m^3$/s of flow rate. |
| Zahhad et al. [5] | CJI cooling for the HCPV-T systems | Tcell was maintained at 65 °C with 6 °C of temperature uniformity using water at $\dot{m}$ = 50 g/min for CR = 1000 |
| Gupta et al. [4] | CJI cooling for HCPV-T system with channel configurations | Five channel configurations were proposed for minimal pressure drop and maximum temperature uniformity. Tcell was reduced to 55 °C under CR = 1000 with a pressure drop of 163 Pa |
| Tang et al. [29] | Ultrathin micro pin-fin channel cooling for HCPV-T systems | Tcell was reduced to 51 °C at CR = 1000 at $\dot{m}$ = 3 kg/h. Pressure drop was 2.73 kPa, and 5.29 kPa for circular and square pin-fin design at $\dot{m}$ = 1.5 kg/h |
| Shohdy et al. [30] | Trimmed fins microchannel cooling for HCPV systems | Temperature uniformity was 20.6 °C at $\dot{m}$ = 200 g/min for HCPV system under CR = 2500 |

**Table 2**
Dimensions of the solar cell, heat sink, and DBC assembly.

| Layer | Length (mm) | Thickness (mm) | Width (mm) |
|---|---|---|---|
| Aluminium heat sink | 150 | 12 | 150 |
| Ceramic | 150 | 0.32 | 150 |
| Copper-1 and 2 | 150 | 0.25 | 150 |
| Germanium | 70 | 0.19 | 70 |
| TEG modules | 20 | 3 | 20 |

**Table 3**
Thermophysical properties of the system [41,42].

| Layer | Emissivity ($\varepsilon$) | Density ($\rho$) (kg/$m^3$) | Specific heat ($C_p$) (J/kg·K) | Thermal conductivity ($k$) (W/m·K) |
|---|---|---|---|---|
| Germanium | 0.9 | 5323 | 320 | 60 |
| Copper | 0.05 | 8700 | 385 | 400 |
| Ceramic | 0.75 | 3900 | 900 | 30 |
| Aluminium | 0.9 | 2719 | 871 | 202.6 |
| TEG module (Bismuth-Telluride) | 0.66 | 4100 | 550 | 1.45 |
| Coolant fluid (water) | – | 998 | 4182 | 0.6 |

## 2. System details

The HCPV-T system comprises a solar cell with a direct bond copper (DBC) assembly. The spectral splitter, solar cell, heat sink with channel configuration, DBC assembly, and thermoelectric generator (TEG) are shown in Fig. 1(a). The solar cell used in this study is a multi-junction solar cell with a reference ηcell of 40.3 % at a reference temperature of 298 K [38]. The dimensions of the solar cell are 70 × 70 mm with an optical efficiency of 90 %. A copper-ceramic-copper assembly of 150 × 150 mm is placed to support the solar cell. An aluminium heat sink of 150 × 150 mm with a thickness of 12 mm, is positioned beneath the DBC assembly to absorb the heat produced by the solar cell. CJI cooling is used to dissipate this heat. Inside the heat sink, channels are designed so

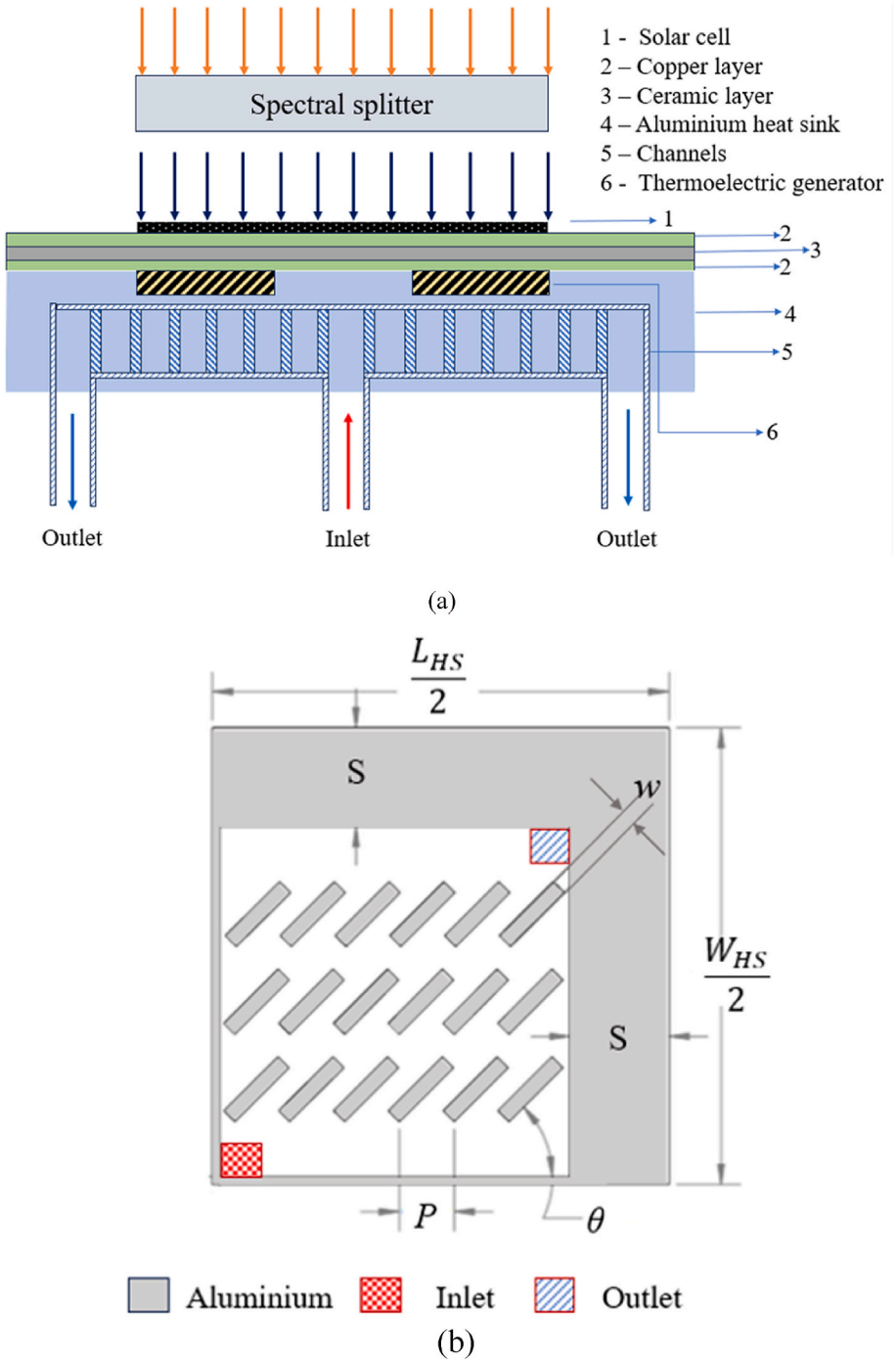



**Fig. 1.** (a) HCPV-T system with confined jet impingement and thermoelectric generator, (b) Channel configuration inside the aluminium heat sink.

that the cooling fluid flows directly to the centre of the heat sink surface and exits through four outlets located at each corner. The channel depth inside the aluminium heat sink is 4 mm. Four thermoelectric generators (TEG) are placed between the DBC assembly and the aluminium heat sink. The dimensions of the TEGs are taken as 20 × 20 mm with 3 mm thickness [39]. The TEGs are placed inside the aluminium heat sink so that the top surface of all the TEGs is attached to the bottom copper layer of the DBC assembly. The bottom surface and sides of the TEGs are in contact with the aluminium heat sink. A spectral splitter is placed over the top surface of the PV cell. The spectral splitter allows a fraction of solar radiation in the 300–1100 nm wavelength range to transmit through the splitter [32].

The solar radiation incidents on the spectral splitter. The photons in the 300–1100 nm wavelength range have very high energy and can cause the electron-hole pair of the solar PV cell to be partially converted into electricity. Hence, the transmissivity of the spectral splitter for 300–1100 nm wavelength radiation is very high. The photons above the 1100 nm wavelength have low energy and cannot generate electricity. Hence, the spectral splitter has high reflectivity for the photons above 1100 nm wavelength [32]. There is a gap between the spectral splitter and the top surface of the PV cell [40]. Hence, the effect of the temperature of the spectral splitter on the performance of the HCPV-T system is not considered in this study. The PV cell absorbs concentrated solar irradiation within the 300–1100 nm wavelength range. A portion of this solar energy is converted into electrical energy through the photovoltaic effect, with the generated power depending on the ηcell,

which is influenced by Tcell. However, the other portion of the solar energy is converted into heat, raising the Tcell. This heat is conducted to the aluminium heat sink via the DBC assembly, and the coolant fluid in the CJI cooling system removes the accumulated heat through convection.

This study investigates various channel configurations by adjusting the fin angle, fin width, and pitch through a systematic design process, as discussed later. Channels are embedded within the aluminium heat sink, with the water jet targeting the heat sink surface at the centre and leaving at the corners of each channel configuration. A schematic of the channel configuration in the heat sink is shown in Fig. 1(b). Where fin angle, fin width, and pitch are denoted by θ, w, and P, respectively. LHS, and WHS are the length and width of the heat sink, respectively. S is taken as 16.5 mm for all channel configurations. Fin angles of 0°, 30°, 45°, 60°, and 75° are tested, along with fin widths of 1.5 mm, 2 mm, and 2.5 mm. Pitches of 7.5 mm and 9 mm are also used. Table 4 provides detailed descriptions of the channel configurations. Both outlets and inlets have a rectangular cross-section measuring 5 mm × 5 mm, and water is used as the coolant in this study.

The dimensions and thermophysical properties of the solar cell and layers are given in Tables 2 and 3, respectively.

## 3. Governing equations

This study considers a 3-D model comprising the solar cell, DBC assembly, aluminium heat sink, and TEG module. A uniform solar irradiation distribution across the 70 × 70 mm PV cell surface is assumed in the numerical model. A 150 × 150 mm aluminium heat sink is positioned behind the solar cell and DBC assembly. The thermophysical properties of the PV cell, DBC assembly, and the TEG module are assumed to be constant. The coolant flow within the heat sink channels is assumed to be steady, incompressible, and behaves as a Newtonian fluid. The flow has a maximum Reynolds number of 2000, indicating a laminar regime based on channel width. A 20 × 20 mm TEG module is installed between the DBC assembly's bottom layer and the aluminium heat sink. In the energy equation, a heat source term is included for both the PV cell and TEG module: for the PV cell, this term depends on $T_{cell}$ and $\eta_{cell}$, while for the TEG module, it is determined by the temperatures at the hot and cold junctions.

### 3.1. For solar cell and DBC assembly

The heat conduction equation across the PV cell layers is as follows [43]:

$$k_i \nabla^2 T_i + q_i = 0 \tag{1}$$

where, $i$th layer thermal conductivity is denoted by $k_i$. The internal heat generation, $q_i$ is assumed to be zero in all layers except Ge. The heat generated in the Ge layer is [43]:

$$q_{Ge} = \frac{(1-\eta_{cell})\cdot G\cdot \alpha_{Ge}\cdot A}{V} \tag{2}$$

where, the absorptivity of the Ge layer is denoted by $\alpha_{Ge}$. The net concentrated irradiation on the solar cell surface is denoted by $G$. The cell surface area and volume are denoted by $A$, and $V$, respectively. The cell electrical efficiency is denoted by $\eta_{cell}$. The $\eta_{cell}$ of the solar PV cell depends on the operating $T_{cell}$. ($1$-$\eta_{cell}$) represents the fraction of the solar energy that is transformed into heat energy. Hence, this fraction of the solar energy is responsible for the heat generation in the solar PV cell.

The net concentrated solar radiation is given as:

$$G = I\cdot CR\cdot \eta_{opt} \tag{3}$$

where, the solar irradiation after passing through the spectral splitter is denoted by $I$. $I$ is assumed to be uniformly distributed on the PV cell surface. $CR$ is the concentration ratio, and $\eta_{opt}$ is the optical efficiency of the solar cell. The optical efficiency of the PV cell is taken as 0.9.

The electrical efficiency of the solar cell ($\eta_{cell}$) is a function of the $T_{cell}$. It is expressed using the following equation:

$$\eta_{cell} = \eta_{ref} - \beta_T\left(T_{cell} - T_{ref}\right) \tag{4}$$

where, cell reference efficiency $\eta_{ref}$ at $T_{ref}$ = 298 K and $CR$ = 1000 is taken as 40.3 %, and $\beta_T$ is the thermal coefficient and is considered as 0.047 % [38].

For coolant fluid flow and heat transfer:

The flow is considered steady and incompressible, with thermophysical properties assumed to be isotropic and unaffected by temperature variations. The fluid flow is considered as Newtonian.

Continuity equation:

$$\rho_f \nabla\left(\vec{V}\right) = 0 \tag{5}$$

Momentum equation:

$$\rho_f\left(\vec{V}.\nabla\vec{V}\right) = -\nabla P + \mu\nabla^2\ \vec{V} \tag{6}$$

Energy equation:

$$\rho_f C_{p,f}\left(\vec{V}.\nabla T\right) = k_f \nabla^2 T \tag{7}$$

where, $k_f$ represents the coolant thermal conductivity, $\rho_f$ and $\mu$ are the density and viscosity of coolant, respectively. $P$ is the pressure, and $\vec{V}$ is coolant velocity.

### 3.2. Thermal and electrical energies

The net electric power ($P_{net}$) is expressed as the difference between the total electric power ($P_{el}$) and power loss due to friction ($P_{fric}$). It can be obtained as [44]:

$$P_{el} = \eta_{cell}\cdot G\cdot \alpha_{Ge}\cdot A \tag{8}$$

$$P_{fric} = \frac{\dot{m}}{\rho_f}\Delta P \tag{9}$$

where, the pressure difference across the heat sink is denoted by $\Delta P$.

$$P_{net} = P_{el} - P_{fric} \tag{10}$$

The thermal power, $Q_{th}$ is expressed as [45],

$$Q_{th} = \dot{m}C_{p,f}\left(T_{f,out} - T_{f,in}\right) \tag{11}$$

where, the coolant temperature at the outlet and inlet is denoted by $T_{f,out}$ and $T_{f,in}$, respectively.

The CPV-T system's thermal efficiency is calculated as,

**Table 4**
Channel configurations considered in this study.

| Channel nomenclature | Fin arrangement | Fin angle ($\theta$) (°) | Fin width ($w$) (mm) | Pitch ($P$) (mm) |
|---|---|---|---|---|
| C1 | Inline | 0 | 2.5 | 9 |
| C2 | Staggered | 0 | 2.5 | 9 |
| C3 | Inline | 30 | 2.5 | 9 |
| C4 | Inline | 45 | 2.5 | 9 |
| C5 | Inline | 45 | 2.5 | 7.5 |
| C6 | Inline | 45 | 1.5 | 7.5 |
| C7 | Inline | 60 | 2.5 | 9 |
| C8 | Inline | 60 | 2 | 9 |
| C9 | Inline | 60 | 1.5 | 9 |
| C10 | Inline | 75 | 2.5 | 9 |

$$\eta_{th} = \frac{Q_{th}}{I \cdot CR \cdot \eta_{opt} \cdot A} \tag{12}$$

### 3.3. Evaluation of thermal and electrical exergies

Thermal exergy refers to the potential of thermal energy to perform work, which is constrained by the temperature at which it is available. It can be calculated as follows [46],

$$E_{th} = \dot{m}_f C_f \left(T_{f,out} - T_{f,in}\right)\left(1 - \frac{T_o}{T_m}\right) \tag{13}$$

where, LMTD is denoted by $T_m$ and is obtained using:

$$T_m = \frac{\left(T_{f,out} - T_{f,in}\right)}{\ln\left(\frac{T_{f,out}}{T_{f,in}}\right)} \tag{14}$$

In equation (13), the reference temperature is denoted by $T_o$ and is equal to 25 °C.

The electrical energy, on the other hand, can be fully utilised. Hence, the $P_{net}$, representing the difference between generated electrical energy and frictional loss, is treated as electrical exergy.

### 3.4. Evaluation of thermal stress

The CTE are different for the Cu and Ge layers. The temperature difference between different layers leads to thermal stress between layers. The thermal stress can be expressed as [47,48]:

$$\sigma_T = E_{Ge} \cdot \Delta\alpha_T \cdot \frac{(T_R\text{-}T)}{(1\text{-}\nu_{Ge})} \tag{15}$$

$$\text{and, } \Delta\alpha_T = \alpha_{T,Ge}\text{-}\alpha_{T,Cu} \tag{16}$$

Where, $\alpha_{T,Ge}$ and $\alpha_{T,Cu}$ are the CTE of Ge and Cu, respectively. $E_{Ge}$ is Young's modulus of the Ge layer. The reference temperature is denoted by $T_R = 25$ °C. $\nu_{Ge}$ is the Ge layer Poisson ratio. The values of the constants are given in Table 5.

The Cu layer has a higher CTE than the Ge layer, resulting in compressive stress in the Cu layer and tensile stress within the Ge layer. Due to the absence of slip between these two layers, they act as beams that can undergo both bending and axial deformations. The curvature of the resulting bent structure is expressed as:

$$\Gamma = \frac{1}{R} = \frac{\left(\alpha_{T,Cu} - \alpha_{T,Ge}\right)\Delta T}{\frac{H}{2} + \frac{2(E_{Ge}I_{Ge} + E_{Cu}I_{Cu})}{h}\left(\frac{1}{w_{Cu}t_{Cu}E_{Cu}} + \frac{1}{w_{Ge}t_{Ge}E_{Ge}}\right)} \tag{17}$$

where, $I_{Cu}$ and $I_{Ge}$ are the MOI of the Cu and Ge layers, respectively. $\Delta T$ is the difference between $T_{cell}$ and $T_{ref}$. $t_{Cu}$ and $t_{Ge}$ are the Cu and Ge layers thickness, respectively. $H$ is the combined thickness of both layers. $w_{Ge}$ and $w_{Cu}$ are the Ge and Cu layers' widths, respectively. The bending stress in the Ge layer can be calculated using:

$$\frac{\sigma_b}{y} = \frac{M}{I} = \frac{E}{R} \tag{18}$$

where, $M$ is the bending moment, $\sigma_b$ is the bending stress, and the radius of curvature is denoted by $R$ for the Ge layer.

**Table 5**
Properties of Ge and Cu layer [49].

| $\alpha_{T,Ge}$ ($K^{-1}$) | $\alpha_{T,Cu}$ ($K^{-1}$) | $E_{Ge}$ (GPa) | $E_{Cu}$ (GPa) | $\nu_{Ge}$ | $\nu_{Cu}$ |
|---|---|---|---|---|---|
| $6.1 \times 10^{-6}$ | $17 \times 10^{-6}$ | 102.7 | 110 | 0.28 | 0.34 |

### 3.5. Performance evaluation criterion (PEC)

The performance of the HCPV-T model with channel configurations is compared with the base cooling case, where the entire heat sink is treated as a cooling medium. The outlet temperature of the cooling fluid ($T_{out}$), cell maximum temperature ($T_{\max}$), and pressure drop ($\Delta P$) across the heat sink are used to calculate PEC and compare the thermal and hydrodynamic performance of the HCPV-T system. $T_{\max}$ is incorporated in the equation to include the electrical performance of the HCPV-T system in PEC. The PEC is expressed as follows [50]:

$$PEC = \frac{\left(\frac{T_{out} - T_{in}}{T_{max} - T_{in}}\right)_{channel}}{\left(\frac{T_{out} - T_{in}}{T_{max} - T_{in}}\right)_{base}} \times \left(\frac{\Delta P_{base}}{\Delta P_{channel}}\right)^{1/3} \tag{19}$$

### 3.6. TEG model

The temperature distribution in the TEG is modelled as:

$$k\nabla^2 T - P_{gen} = 0 \tag{20}$$

where, $P_{gen}$ is the TEG power generation per unit volume. The TEG power generation can be estimated as:

$$P_{TEG} = Q_h - Q_c \tag{21}$$

$$P_{TEG} = P_{gen} \times V_{TEG} \tag{22}$$

where, the heat input and output from the TEG module are denoted by $Q_h$ and $Q_c$. The TEG volume is denoted by $V_{TEG}$.

The amount of heat input and heat output associated with the TEG module is expressed as follows [51,52]:

$$Q_h = n \cdot \varepsilon_t \cdot I_g \cdot T_h + K \cdot \Delta T - \frac{1}{2} I_g{}^2 R \tag{23}$$

$$Q_c = n \cdot \varepsilon_t \cdot I_g \cdot T_c + K \cdot \Delta T + \frac{1}{2} I_g{}^2 R \tag{24}$$

where, $n$ is the number of p-n units in the TEG module. The number of p-n units in the TEG module is taken as 128. $\varepsilon_t$ is the mean Seebeck coefficient of the TEG module. The Seebeck coefficient of the TEG module is taken as 282 μV/K. $T_h$ and $T_c$ are the temperatures of the hot and cold junctions of the TEG module, respectively. $I_g$ is the electric current in TEG, and $R$ is the electrical resistance of the TEG module. $\Delta T$ is the temperature difference between the hot and cold junctions of the TEG module.

The electric current and electrical resistance of the TEG module can be calculated using the following equation [42,53].

$$I_g = \frac{n \cdot \varepsilon_t \cdot (T_h - T_c)}{R(1 + \mu)} \tag{25}$$

$$R = 10^{-5} \times (-3)(T_m - 273)^2 - 0.0133(T_m - 273) + 1.542 \tag{26}$$

where, $\mu$ is defined as the ratio of load resistance to the internal resistance, and $T_m$ is the mean temperature of the hot and cold junction temperature of the TEG module.

The electrical efficiency of the TEG module is given using the following equation [52]:

$$\eta_{TEG} = \frac{I_g{}^2 \cdot R_L}{Q_h} \tag{27}$$

where, $R_L$ is the load resistance.

### 3.7. Boundary conditions

Convective and radiative boundary conditions are given at the top surface of the Cu and Ge layers. Convective boundary conditions are also specified for all sides of the Ge layer, heat sink, and DBC assembly. All the interfaces are given thermally coupled boundary conditions. Coolant inlet temperature is considered uniform, and normal velocity conditions are given, while the outlet is set to zero-gauge pressure. For the top surface of the system exposed to the ambient,

$$-k_{Ge}\frac{\partial T_{Ge}}{\partial z} = q_{rad,Ge\to S} + q_{conv,Ge\to a} \tag{28}$$

$$-k_{cu}\frac{\partial T_{cu}}{\partial z} = q_{rad,cu\to S} + q_{conv,cu\to a} \tag{29}$$

where, $q_{rad,Ge\to S}$ is the losses due to radiation from the Ge cell and $q_{conv,Ge\to a}$ is the heat losses due to convection from the Ge cell layer to the ambient.

The heat losses due to convection from the Ge layer can be calculated using [41]:

$$q_{conv,Ge\to a} = h_{conv,wind}(T_{Ge} - T_a) \tag{30}$$

$$h_{conv,wind} = 5.82 + 4.07V_{wind} \tag{31}$$

where the ambient temperature is denoted by $T_a$, $T_{Ge}$ is the temperature of the top surface of the Ge cell, the wind velocity is denoted by $V_{wind}$, and the convective HTC is denoted by $h_{conv,\ wind}$.

The heat losses due to radiation from the Ge layer can be calculated using [41]:

$$q_{rad,Ge\to S} = \sigma\epsilon_{Ge}\left(T_{Ge}^4 - T_s^4\right) \tag{32}$$

$$T_s = 0.0522T_a^{1.5} \tag{33}$$

where, the Ge layer emissivity is denoted by $\varepsilon_{Ge}$, and the sky temperature is denoted by $T_s$ in Kelvin.

At the interfaces between the solar cell, DBC assembly, heat sink and TEG,

$$-k_m\nabla T_m = -k_n\nabla T_n \text{ and } T_m = T_n \tag{34}$$

At the heat sink inlet: $V_f = V_{in}$ and $T_{in} = 298$ K

At heat sink outlet: $P_{out} = 0$ Pa.

No slip boundary condition is given at the fluid-solid interface.

The sides and bottom of the aluminium heat sink are subjected to convective boundary conditions. Equation (30) calculates $h_{conv,\ wind}$ and is estimated to be 9.79 W/m$^2$-K.

In this study, the governing equations are solved using the 2020 R2 version of ANSYS Fluent. To discretize the momentum, continuity, and energy equations, a second-order upwind scheme is implemented along with the coupled algorithm. The convergence criteria are set at $10^{-3}$ for continuity, $10^{-6}$ for momentum, and $10^{-8}$ for energy. A user-defined function (UDF) is incorporated to include the source term for the PV cell and TEG module in the energy equation. The heat generation in the PV cell is incorporated as per equations (1), (2) and (4). The voltage generated due to temperature difference across the TEG (Seebeck effect) is modelled using a source term in the energy equation. Internal resistive heating (Joule heating) is implemented in the UDF as a volumetric heat generation. The formulations for TEG source terms are taken as per equations (21), (23) and (24). Initially, the ANSYS Fluent solves flow and temperature fields. The temperature-dependent electrical outputs and source terms are calculated using the UDFs. These values feed back into the energy equation for the next iteration. The UDF is executed at each iteration to update source terms based on the local temperature distribution.

## 4. Grid sensitivity test

A grid-sensitive test is conducted for each channel configuration to evaluate the effect of grid size on the results. The average cell temperature is monitored across various grid sizes. Fig. 2(a) shows the isometric view of the meshed geometry. As shown in Fig. 2(b), the relationship between $T_{cell}$ and the number of elements for channel configuration C5 is displayed. The results indicate that beyond 10 million elements, the cell's average temperature remains effectively unchanged. The variation in average temperature falls below 0.1 % for grid sizes exceeding 10 million elements, indicating that this difference is minimal and negligible.

## 5. Validation of the solar cell model, TEG model, and flow model

The numerical model for the PV cell used in the study is validated with the results obtained by Zahhad et al. [5]. The effect of a CJI cooling system on the performance of the HCPV-T system was studied by the authors. Fig. 3(a) depicts the solar cell model validation with the results presented by Zahhad et al. [5] with a maximum error of 1.8 %. Fig. 3(b) shows the TEG model validation with the datasheet as provided by the TEG manufacturer [42] at a constant cold junction temperature of 30 °C. It can be observed that the TEG model predicts electric power generation with less than 6 % error in the temperature range of 50 °C–80 °C. However, the thermophysical properties and the Seebeck coefficient of the TEG are assumed to be constant in the current study. This leads to an increase in errors at the high-temperature difference between TEG junctions, increasing the difference between the current study and experimental data to around 11 % in the temperature range of 90 °C–110 °C. Fig. 3(c) and (d) illustrate the validation of the flow model by comparing the pressure drop across the heat sink and the average heat transfer coefficient with experimental data reported by Barrau et al. [28]. The results indicate that the flow model predicts the pressure drop and average heat transfer coefficient with maximum errors of 6.4 % and 4.5 %, respectively. The surface roughness of the channels is not considered in this study. The side and bottom walls of the heat sink are given adiabatic boundary conditions. It leads to an error in pressure drop and HTC validation.

## 6. Results and discussion

The effect of the CJI cooling and thermoelectric generator on the HCPV-T system performance is shown in the present study. A 150 × 150 mm heat sink is placed on the backside of the DBC assembly. The channels are created inside the aluminium heat sink. Four TEG modules of dimension 20 × 20 mm are placed between the DBC assembly and the aluminium heat sink. The TEG modules are placed such that the hot junction of the TEG modules is in contact with the copper layer of the DBC assembly. The sides and the cold junction of the TEG modules are in contact with the aluminium heat sink. Mixed radiation and convection boundary conditions are given to the Ge layer and the top Cu layer's upper surface, which are exposed to the environment. Convective conditions are given to all sides of the PV cell, DBC assembly, and heat sink. The Reynolds number is kept constant for all the channel configurations and is taken as 2000. A summary of the effect of the channel configurations on the various performance parameters of the HCPV-T system is shown in Table 6.

### 6.1. Cooled conditions

The hybrid cooling technique in the present study consists of a CJI cooling technique and the TEG module, which uses waste heat to generate extra electrical energy. The effect of the different parameters of channel configuration, such as fin angle, fin width, fin pitch, and HCPV-T system performance, is studied. At CR = 1000, the two-dimensional temperature maps at the top surface of the cell for the different fin

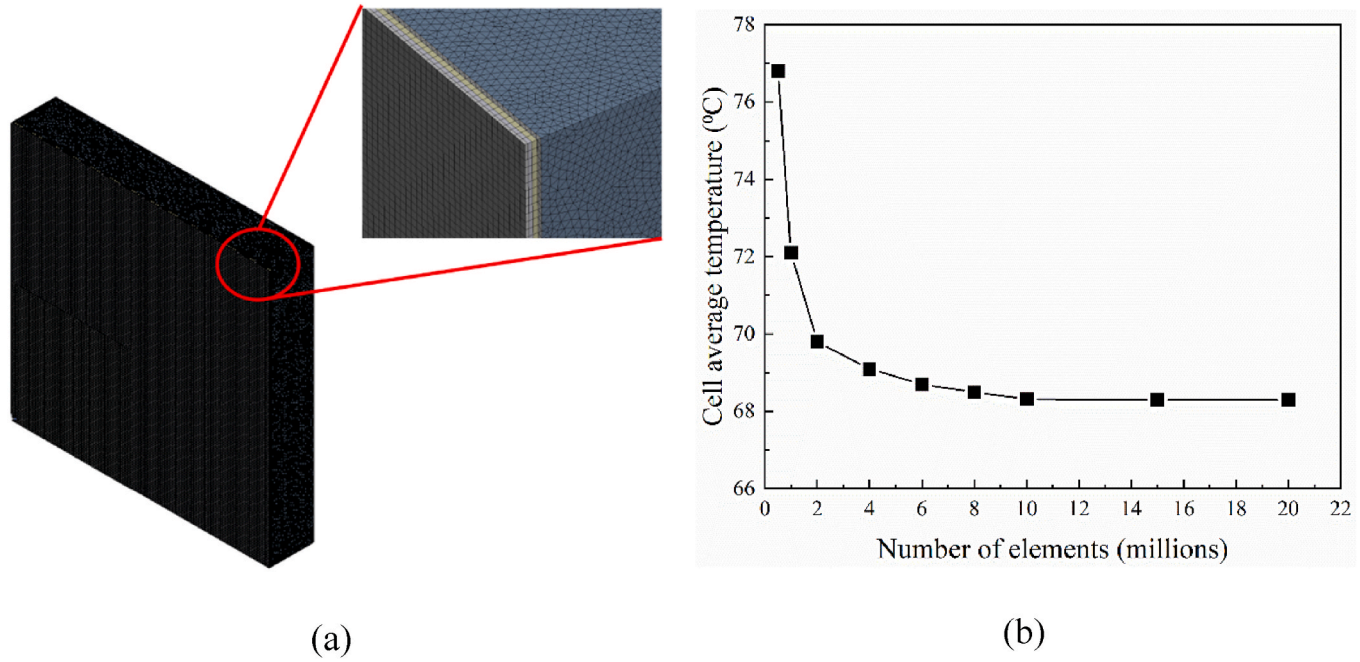



**Fig. 2.** (a) Meshed geometry, (b) grid independence test for configuration C5.

angles, fin width, and pitch are shown in Fig. 4. It is observed that the maximum temperature occurs at the locations where the TEG modules are placed. The low thermal conductivity of the TEG modules results in a higher thermal resistance at those locations. It leads to lower heat conduction from the PV cell to the aluminium heat sink at TEG locations. The temperature is non-uniformly distributed on the top of the PV cell. The temperature is observed to be minimal at the sides and corners of the PV cell since the sides are exposed to ambient. The water jet impinges at the centre of the PV cell. The kinetic energy of the jet converts into the pressure energy at the point of impingement. Hence, the HTC is maximum at the cell centre, resulting in a lower temperature. However, the temperature of the cell increases along the centre and diagonal lines of the cell. The heat conduction from the PV cell to DBC layers and aluminium heat sink is maximum at the cell centre due to lower thermal resistance. The lower thermal conductivity of the TEG modules results in a gradual increase in thermal resistance along the centre and diagonal lines of the cell surface. It results in an increase in cell temperature away from the PV cell centre. It can be noted that the maximum temperature over the PV cell surface is within the permissible limits of 110 °C except for configurations C1, C2, C3, C6, and C9. The maximum $T_{cell}$ is higher with channel configurations C1 and C2 due to the flow maldistribution with 0° fin angles. Due to higher flow resistance in the channel path, the fluid does not flow over the TEG locations in configurations C1 and C2. Hence, the maximum cell temperature increases at TEG locations for configurations C1 and C2. The channel configuration C3 also suffers from a flow maldistribution in the channel path due to lower fin angles, resulting in a higher maximum temperature of the cell. The maximum temperature for channel configurations C6 and C9 is higher than 110 °C due to the 1.5 mm fin width for these configurations. The lower fin width results in lower heat conduction in the aluminium heat sink. Fig. 4(j) shows that the cell temperature is minimal with channel configuration C10. This can be attributed to the increased local velocity and vortex stretching phenomenon in configuration C10, which will be discussed in subsequent sections.

Fig. 5 shows the contours of velocity over the parallel sectional plane of the coolant fluid domain for all the channel configurations at Re = 2000 and $CR = 1000$. The velocity of the coolant is the maximum at the entrance of the jet. The kinetic energy of the jet converts into pressure energy at the point of impingement, resulting in a maximum HTC at the PV cell centre. The boundary layer is thinnest at the impingement point and gradually grows as the coolant flows along the channel path, leading to a reduction in HTC. Therefore, an increase in temperature over the cell surface away from the centre can be observed. However, the fin-induced disturbances partially disrupt the boundary layer growth, causing enhanced heat transfer near the fins. From Fig. 5(a) and (b), it can be seen that there is a flow maldistribution in the channel path for channel configurations C1 (inline fin) and C2 (staggered fin), where the fin angle and the fin number are same (0° and 21, respectively). The flow resistance between the fins is significantly high in channel configurations C1 and C2. This prevents the coolant fluid from passing over the hotspot zone; instead, the fluid flows through the peripheral passages. As a result, the temperature of the PV cell at the TEG locations is higher than 110 °C for channel configurations C1 and C2. Hence, in the next study, the fin angle of configuration C1 is increased to 30° (configuration C3) to allow the fluid to flow through the hotspots for effective cooling. As the fin angle increases, the flow resistance in the peripheral channels increases, which results in the fluid flowing between the fin gaps over the hotspot zones. Hence, the cell maximum temperature for configuration C3 reduces with the increased fin angle. Further increases in the fin angle to 45° (configuration C4), 60° (configuration C7), and 75° (configuration C10) show a decrease in the cell's maximum temperature. However, the increase in fin angle results in an increase in pressure drop across the channel. Hence, the fin angle is fixed at 45°, and the fin pitch is varied to 7.5 mm (configuration C5). By comparing configurations C4 and C5, it can be observed that the pitch between fins has a crucial role in flow patterns and cell temperature. The flow pattern is more uniform with configuration C5 than C4. It results in better temperature uniformity over the PV cell surface. A smaller pitch results in a reduced channel width, leading to an increase in the local coolant velocity. As a result, a drop in cell temperature and an increase in pressure drop are observed. In order to observe the fin width, configuration C6 is developed, where the fin width is reduced to 1.5 mm. It is found that the $T_{max}$ is increased because of the reduction in local HTC due to a decreased channel Reynolds number. Similar effects of increased cell maximum temperature have been observed for configurations C8 (fin angle = 60°, fin width = 2 mm) and C9 (fin angle = 60°, fin width = 1.5 mm). Therefore, it can be concluded that the cell maximum temperature is lower than the permissible limit (110 °C) for

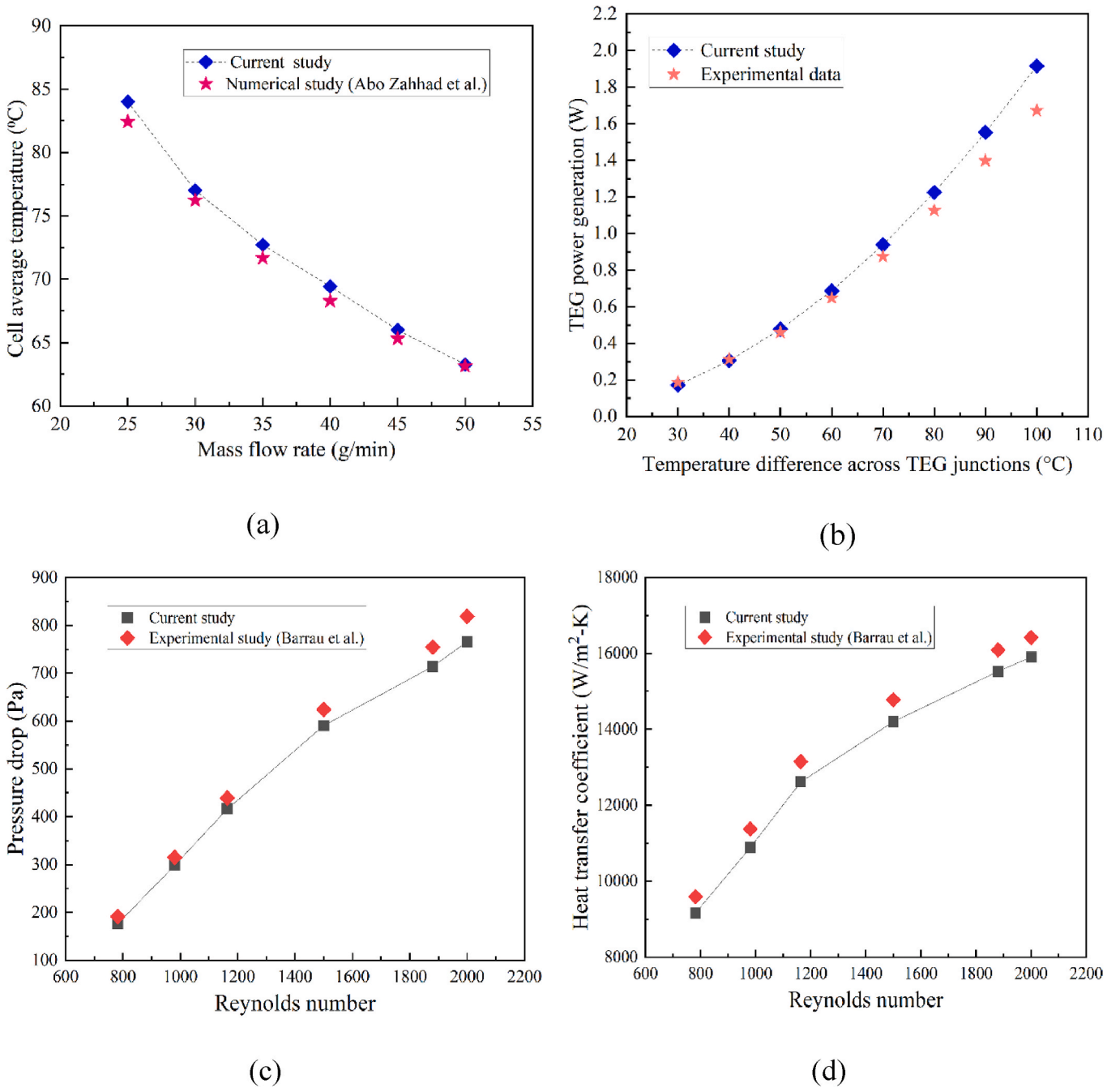



**Fig. 3.** Validation of the (a) solar cell model, (b) TEG model, (c) pressure drop across the heat sink and (d) Average heat transfer coefficient.

**Table 6**
Effect of channel configurations on various performance parameters.

| Channel configuration | $T_{max}$ (°C) | $T_{avg}$ (°C) | $\eta_{cell}$ (%) | $\Delta P$ (Pa) | $\eta_{th}$ (%) | PEC | $\Delta T_{non\text{-}uniformity}$ (°C) | $P_{TEG}$ (W) | $\zeta_o$ (%) |
|---|---|---|---|---|---|---|---|---|---|
| C1 | 115.1 | 74 | 37.9 | 1310 | 55.4 | 1.28 | 65.1 | 4.13 | 52.64 |
| C2 | 112.8 | 72.8 | 38 | 1462 | 55.36 | 0.94 | 65.17 | 3.89 | 52.55 |
| C3 | 111.8 | 71.13 | 38.13 | 1377 | 55.28 | 1.12 | 63.93 | 3.95 | 52.65 |
| C4 | 110 | 70 | 38.18 | 1423 | 55.23 | 1.17 | 63.9 | 3.94 | 52.64 |
| C5 | 108.1 | 68.32 | 38.26 | 1515 | 55.15 | 1.12 | 63.1 | 3.66 | 52.61 |
| C6 | 111.2 | 70.93 | 38.14 | 1360 | 55.27 | 1.17 | 64.03 | 4.1 | 52.67 |
| C7 | 107.8 | 68.3 | 38.26 | 2032 | 55.15 | 1.04 | 63.78 | 3.73 | 52.22 |
| C8 | 108.7 | 69 | 38.23 | 1758 | 55.18 | 1.1 | 63.84 | 3.85 | 52.41 |
| C9 | 110.4 | 70.2 | 38.17 | 1490 | 55.24 | 1.3 | 64 | 4.03 | 52.59 |
| C10 | 107.4 | 67.47 | 38.30 | 15462 | 55.11 | 0.58 | 63.34 | 3.61 | 42.34 |

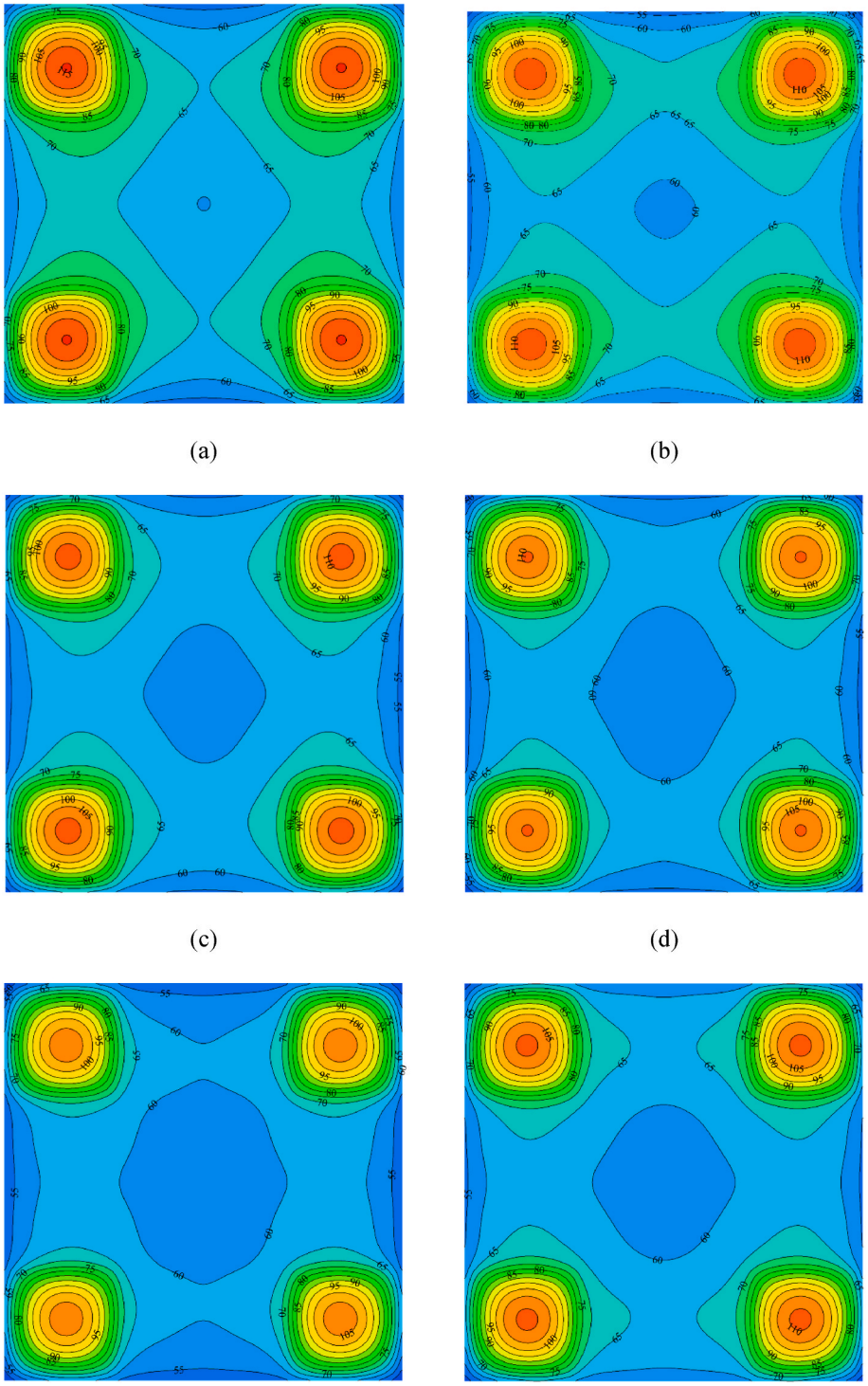



**Fig. 4.** 2-D temperature map at the cell top surface for channel configuration (a) C1, (b) C2, (c) C3, (d) C4, (e) C5, (f) C6, (g) C7, (h) C8, (i) C9, (j) C10.

configurations C4, C5, C7, C8 and C10; however, the pressure drop across the heat sink is the lowest for C4. Hence, a performance evaluation criterion combining the effect of heat transfer and pressure drop is evaluated to ascertain the best-performing heat sink configurations.

Fig. 6 shows the velocity streamlines over the parallel sectional plane of the fluid domain for channel configurations C1, C4, and C10. It has been observed that the internal arrangement of the fins disturbs the incoming flow, leading to the formation of multiple recirculation zones at different locations depending on the fin angle. The creation of these recirculation zones is associated with boundary layer separation. Fig. 6 (a) shows that the zones of higher velocity are created in the peripheral passages of the channel configuration C1. In these regions, the boundary layer remains attached to the wall. Conversely, multiple weaker vortices are formed in the passage between the fins as the major portion of the flow occurs in the peripheral passages, resulting in a lower local heat transfer for channel configuration C1. Fig. 6(b) shows that the streamline pattern becomes more aligned along the 45° inclination for configuration C4. In configuration C4, the upstream fins at incidence

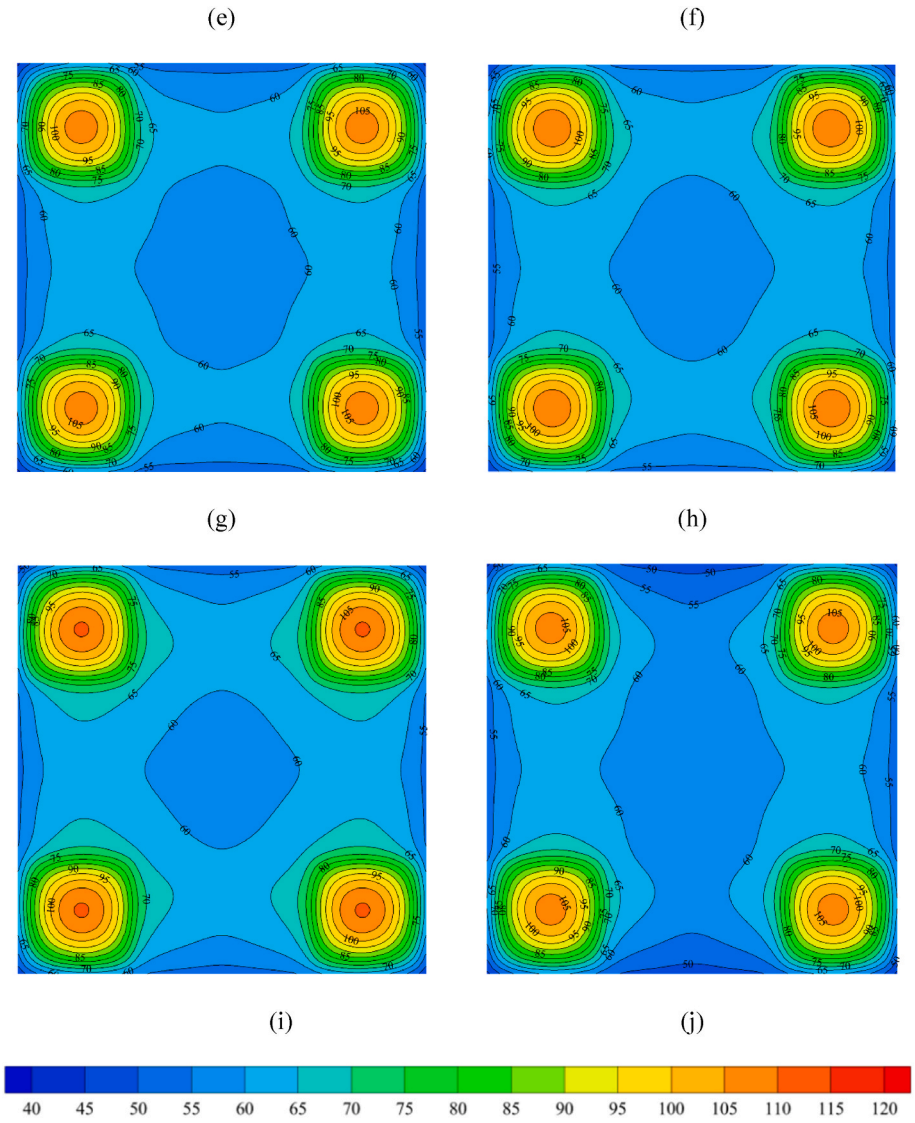



**Fig. 4.** (*continued*).

divide the incoming flow, and the boundary layer develops along the surfaces of the fins and disrupts at the trailing surface of the fins, leading to the mixing of flow. The flow then impinges the downstream staggered fins, forming a vortex at the leading face of each staggered fin. The wake is formed downstream of each staggered fin as the boundary layer starts to separate at the trailing surface of the fin. However, the inclined orientation allows the alignment of these recirculation flows along the direction of the main flow, resulting in an increased local HTC and heat transfer. In Fig. 6(c), significant vortex interactions are observed for configuration C10 with a 75° fin angle. The closely formed, stronger vortices between adjacent fins interact, leading to vortex stretching phenomena. This results in an intensification of vortex strength. These interactions lead to enhanced localized mixing and boundary layer disruption, resulting in enhanced heat transfer between the fins. The enhancement of heat transfer with configuration C10 can also be observed in Fig. 4(j), where the cell temperature is minimal with configuration C10 due to enhanced localized mixing.

Fig. 7(a) shows the effect of different channel configurations on the maximum temperature over the cell surface. The maximum temperature over the cell surface is 115.1 °C, 112.8 °C, 111.8 °C, 110 °C, 108.1 °C, 111.2 °C, 107.8 °C, 108.7 °C, 110.4 °C, and 107.4 °C for channel configurations ranging from C1-C10 respectively. The $T_{max}$ over the cell surface is highest with channel configurations C1 and C2 due to the flow maldistribution in these channel configurations. Channel configurations C6 and C9 have a high maximum cell temperature due to a decreased fin width. Channel configuration C5 results in a lower temperature than channel configuration C4 due to the lower pitch. The maximum temperature over the cell surface is the lowest with channel configurations C7 and C10 due to the increased velocity in these channel configurations. The higher fin angle allows the coolant to pass through the channels with a higher velocity, which results in a higher HTC along the channel path.

Fig. 7(b) shows the effect of different channel configurations on the average temperature of the PV cell. The average temperature of the PV cell is 74 °C, 72.8 °C, 71.13 °C, 70 °C, 68.32 °C, 70.93 °C, 68.3 °C, 69 °C, 70.2 °C, and 67.47 °C for channel configurations ranging from C1-C10 respectively. The $T_{cell}$ is the highest for configuration C1 due to flow maldistribution in the channels and the lowest for channel configuration 10 due to increased velocity in the channels.

### B Cell electrical efficiency and electric power generation

Fig. 8(a) shows the effect of different channel configurations on the cell electrical efficiency ($\eta_{cell}$). The $\eta_{cell}$ is 37.9 %, 38 %, 38.13 %, 38.18 %, 38.26 %, 38.14 %, 38.26 %, 38.23 %, 38.17 %, and 38.30 % for channel configurations ranging from C1 to C10, respectively. The

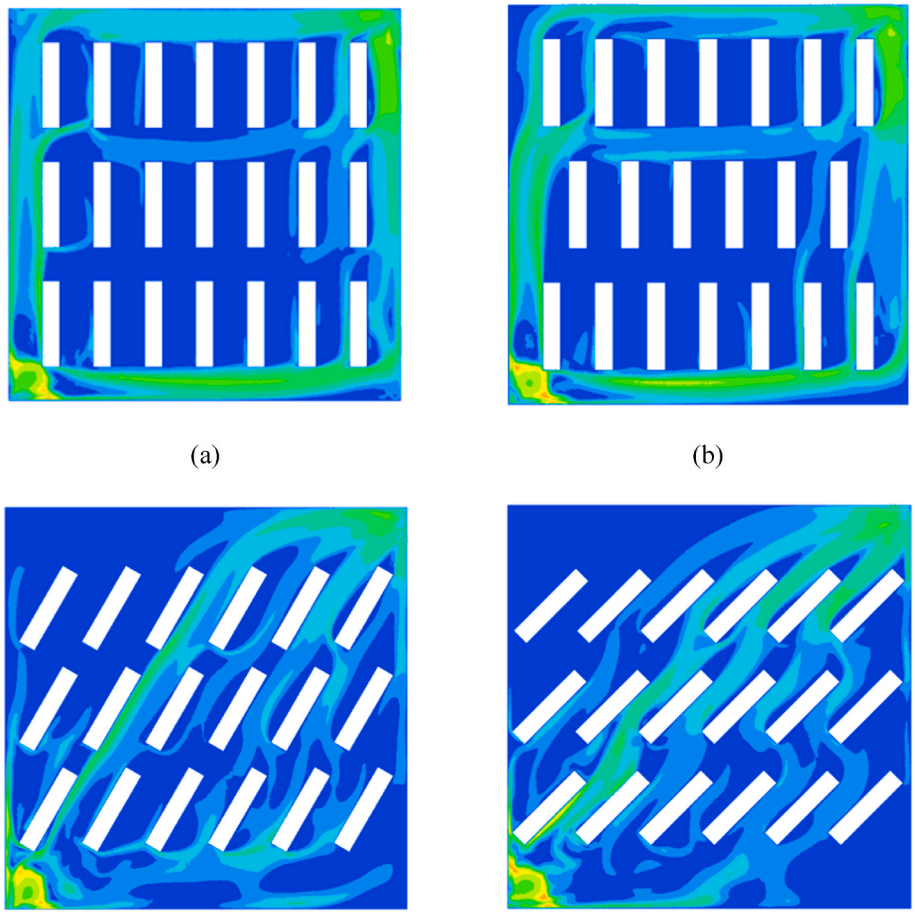



**Fig. 5.** Velocity (m/s) contours on the parallel sectional plane of the coolant fluid domain for channel configurations (a) C1, (b) C2, (c) C3, (d) C4, (e) C5, (f) C6, (g) C7, (h) C8, (i) C9, (j) C10.

electrical efficiency of the PV cell is a function of the cell operating temperature. As the $T_{cell}$ increases, the $\eta_{cell}$ also decreases as a result of a decrease in the open circuit voltage. Hence, the $\eta_{cell}$ is maximum for channel configuration C10 and minimal for channel configuration C1.

Fig. 8(b) shows the effect of different channel configurations on the electrical power generated by the PV cell. The electric power generated by the cell is 1032.2 W, 1033.7 W, 1035.8 W, 1037.3 W, 1039.4 W, 1036.1 W, 1039.5 W, 1038.6 W, 1037 W, and 1040.5 W for channel configurations ranging from C1 to C10, respectively. It is observed that, for a given $I$ and CR, the $P_{el}$ follows the trend of $\eta_{cell}$, i.e., $P_{el} \propto \eta_{cell}$. Hence, the electric power is maximum with configuration C10 and minimal with configuration C1.

C Pressure drop

Fig. 9 shows the effect of channel configurations on the pressure drop across the heat sink. The $\Delta P$ is 1310 Pa, 1462 Pa, 1377 Pa, 1423 Pa, 1515 Pa, 1360 Pa, 2032 Pa, 1758 Pa, 1490 Pa, and 15462 Pa for configurations ranging from C1-C10 respectively. The pressure drop increases sharply for configuration C10. The channel width is reduced in configuration C10 due to the 75° fin angle and inline fin configuration, which increases coolant velocity in the channel. This leads to a high-pressure drop across the heat sink for channel configuration C10. Hence, the frictional power losses for configuration C10 are significantly high, leading to higher pumping power. The $\Delta P$ is minimal with configurations C1, C3, and C6. The $\Delta P$ in channel configuration C2 is higher than in C1 due to the staggered fin arrangement. It has also been observed that the $\Delta P$ with the current channel configurations is significantly lower than those reported by Tang et al. [29] due to mini-scale channel configurations.

D Thermal efficiency

Fig. 10 shows the effect of different channel configurations on the thermal efficiency of the HCPV-T system. The thermal efficiency of the HCPV-T system is 55.4 %, 55.36 %, 55.28 %, 55.23 %, 55.15 %, 55.27 %, 55.15 %, 55.18 %, 55.24 %, and 55.11 % for channel configurations ranging from C1 to C10, respectively. The $\eta_{th}$ is maximum with configuration C1 and is minimal with the C10 configuration. Since the $\eta_{cell}$ is minimal with configuration C1, it leads to a higher fraction of the available energy converted into heat energy. Therefore, configuration C1 enables greater thermal energy extraction by the coolant, leading to an increase in the thermal efficiency of the HCPV-T system.

EPerformance evaluation criterion (PEC):

Fig. 11 shows the performance evaluation criterion (PEC) for different channel configurations. The PEC compares the overall performance of the various channel configurations with the base cooling case, where no channel is introduced in the aluminium heat sink. The PEC factor is 1.28, 0.94, 1.12, 1.17, 1.12, 1.17, 1.04, 1.1, 1.3, and 0.58 for channel configurations ranging from C1 to C10, respectively. The PEC factor is minimal with channel configuration C10 due to a higher pressure drop. The PEC factor is less than one for channel configurations C2 and C10. Hence, the HCPV-T system's overall performance is poor with these channel configurations compared to the base cooling case, where

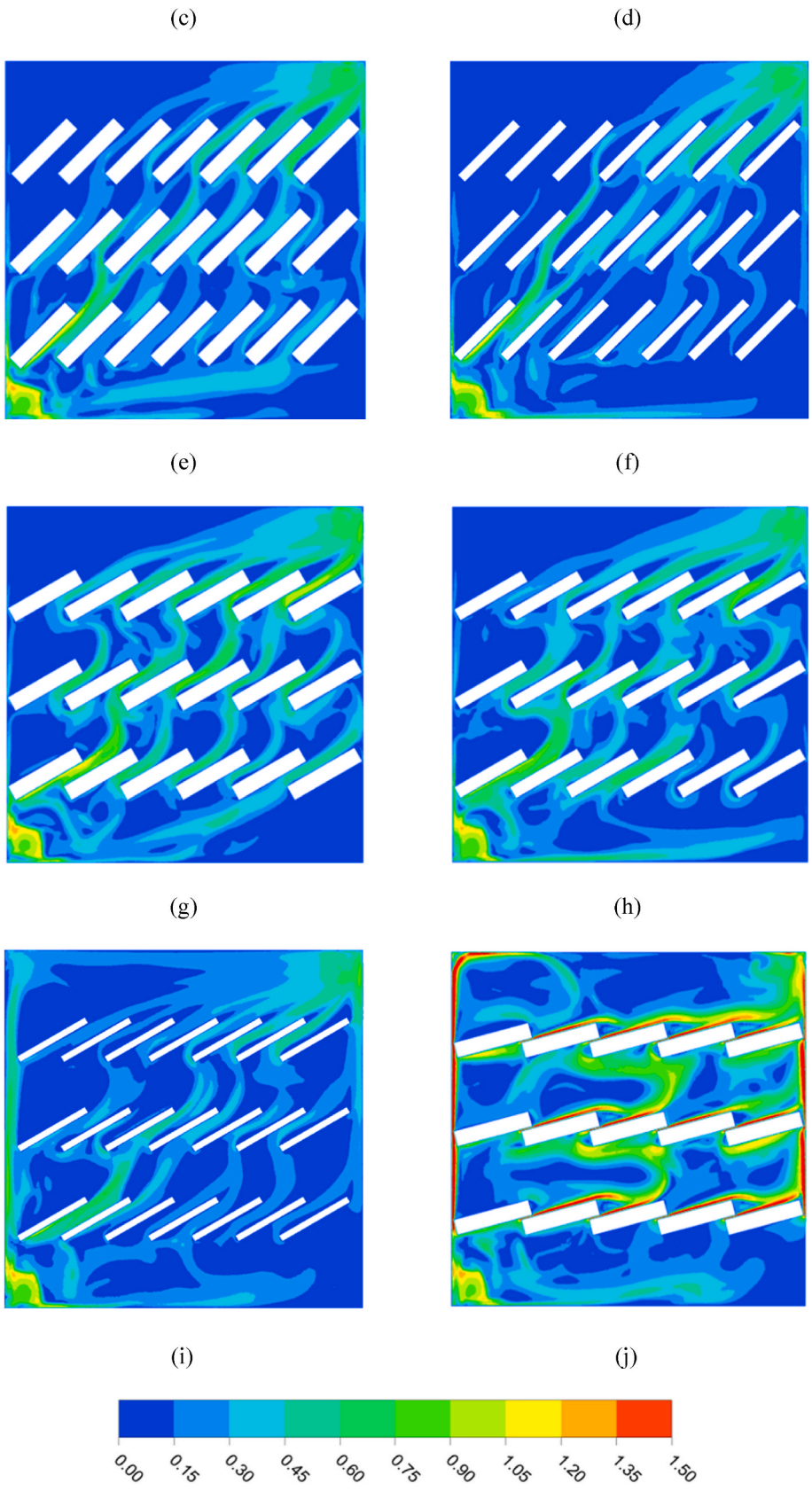



**Fig. 5.** (*continued*).

no channel is introduced in the heat sink. The PEC is highest with channel configurations C1, and C9, followed by C4 and C6. However, the maximum temperature of the cell is beyond the permissible limits of 110 °C with configurations C1, C2, C3, C6, and C9. Hence, these channel configurations cannot be used to cool HCPV-T systems. Therefore, channel configuration C4 provides the highest PEC factor for the cooling

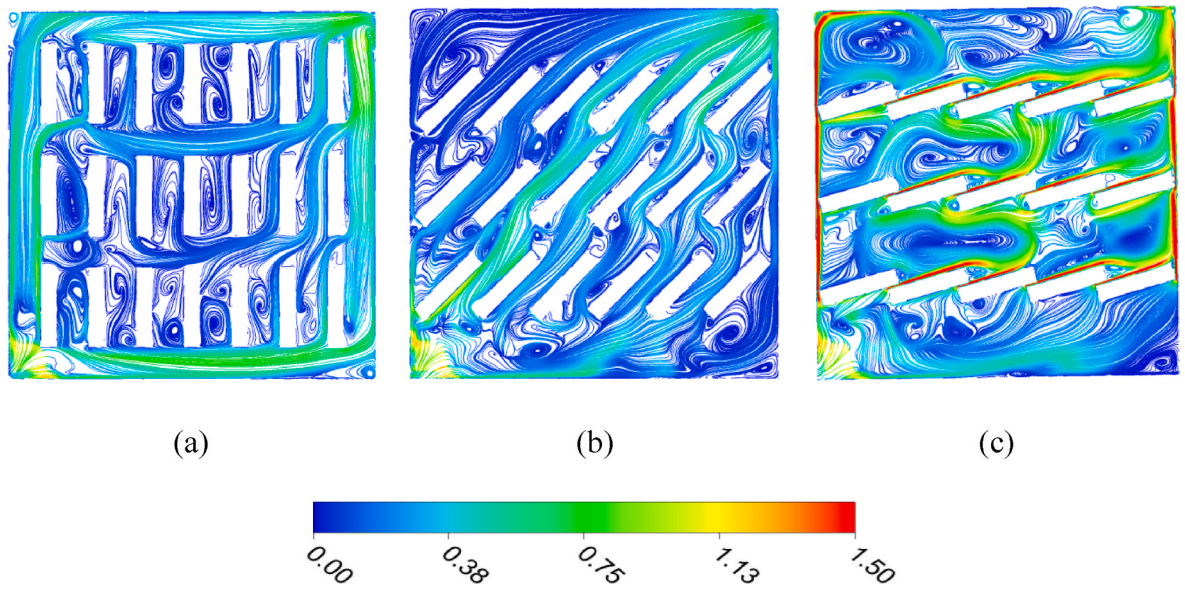



**Fig. 6.** Velocity streamlines contour over the parallel sectional plane of the coolant fluid domain for channel configurations (a) C1 (b) C4 (c) C10 A. Cell temperature.

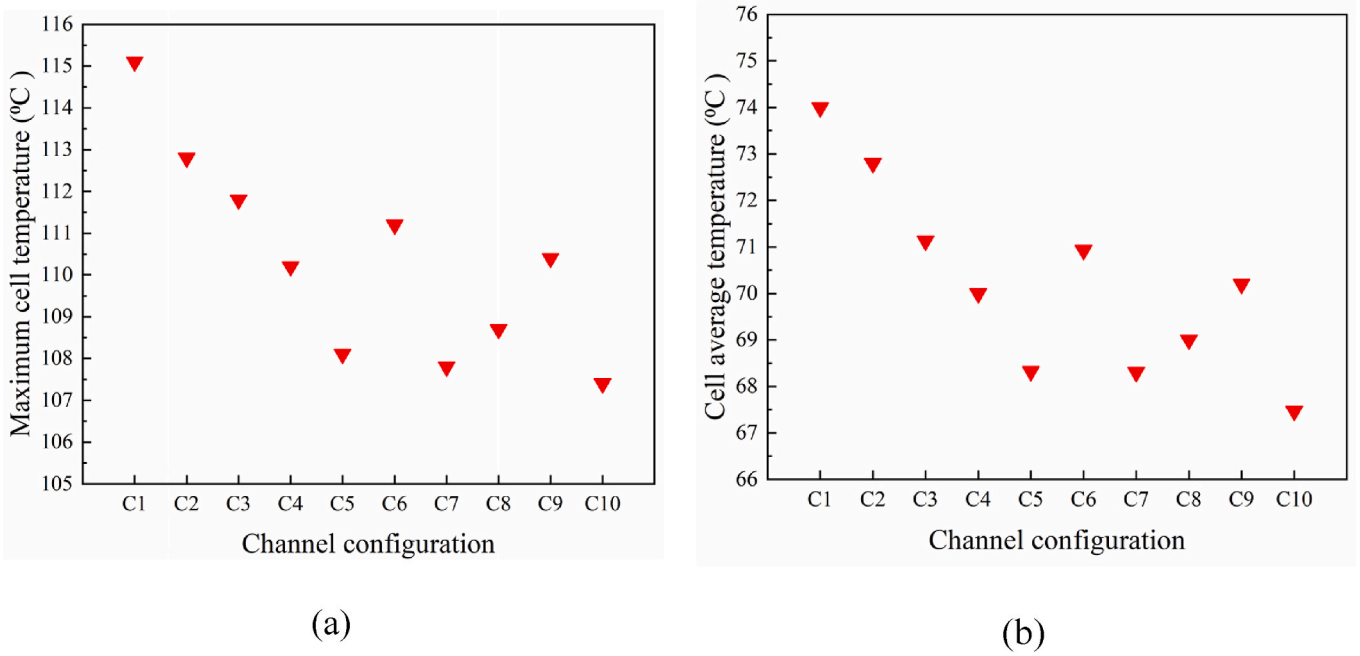



**Fig. 7.** Effect of channel configurations on (a) $T_{max}$ and (b) $T_{cell}$.

of the HCPV-T system.

F Temperature non-uniformity

Fig. 12 shows the effect of various channel configurations on the temperature non-uniformity over the cell top surface. Temperature non-uniformity is the difference between the maximum and minimum temperature across the PV cell surface. The cell temperature non-uniformity is 65.1 °C, 65.17 °C, 63.93 °C, 63.9 °C, 63.1 °C, 64.03 °C, 63.78 °C, 63.84 °C, 64 °C, and 63.34 °C for channel configurations ranging from C1-C10 respectively. The non-uniformity of $T_{cell}$ is maximum with configurations C1 and C2. The coolant fluid does not flow between the channel path for configurations C1 and C2 due to higher flow resistance in the path, as mentioned earlier. It leads to higher HTC at the corners of the channel and lower at the centre of the domain. Hence, the non-uniformity of $T_{cell}$ is higher at the cell top surface. The configuration, C5, provides minimal temperature non-uniformity.

G TEG temperature, resistance, and TEG electrical power

Fig. 13(a) shows the effect of various channel configurations on the temperature difference between cold and hot junctions of the TEG module. The temperature difference between hot and cold junctions of the TEG module is 39.9 °C, 40.2 °C, 41.48 °C, 42.69 °C, 42.14 °C, 43.05 °C, 43.03 °C, 43.3 °C, 43.23 °C, and 42.38 °C for channel configurations ranging from C1 to C10, respectively. The temperature difference across TEG junctions is minimal with configurations C1 and C2 due to flow maldistribution. The coolant fluid does not flow over the cold junction of the TEG module due to high flow resistance. It leads to a higher temperature of the TEG cold junction, resulting in a lower

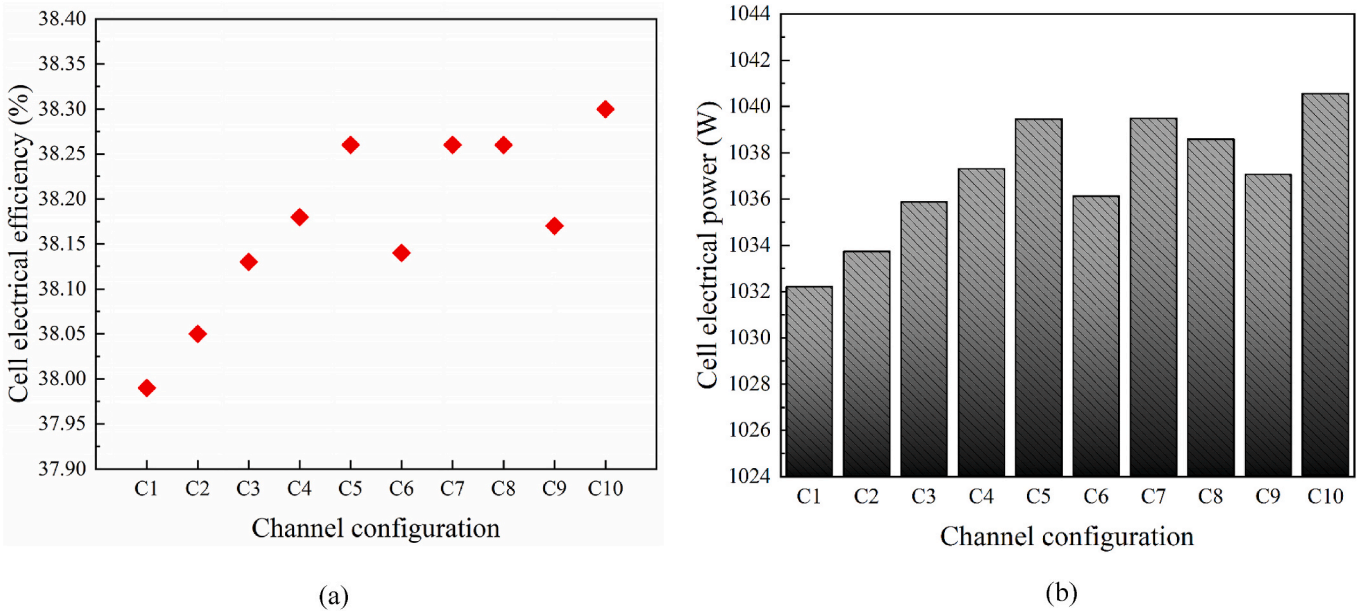



**Fig. 8.** Effect of channel configurations on the (a) cell electrical efficiency, (b) cell electric power.

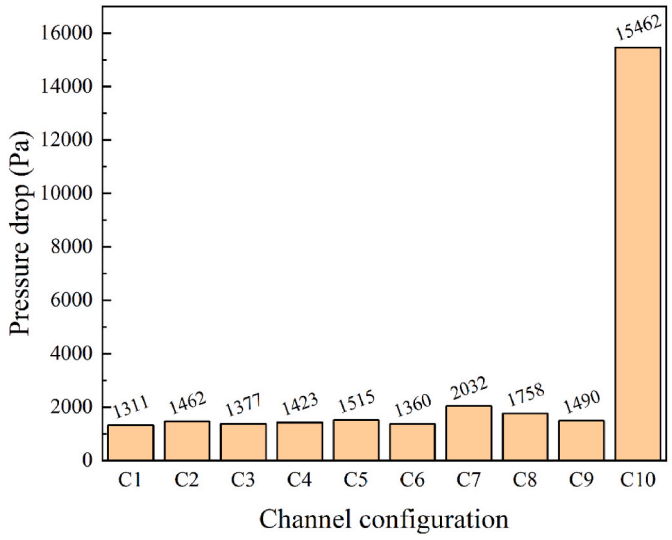



**Fig. 9.** Effect of channel configurations on the pressure drop.

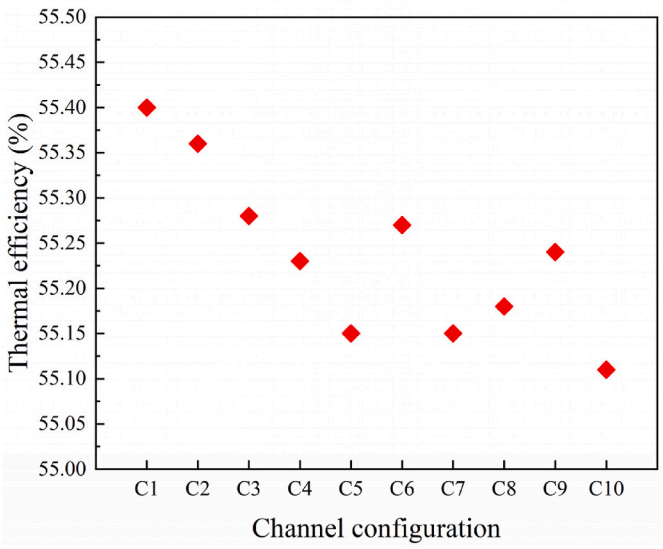



**Fig. 10.** Effect of channel configurations on the thermal efficiency of the HCPV-T system.

temperature difference across junctions.

Fig. 13(b) shows the effect of various channel configurations on the TEG electrical resistance ($R$). The TEG electrical resistance is 0.5 Ω, 0.54 Ω, 0.56 Ω, 0.60 Ω, 0.63 Ω, 0.59 Ω, 0.64 Ω, 0.63 Ω, 0.60 Ω, and 0.64 Ω for channel configurations ranging from C1 to C10, respectively. The electrical resistance ($R$) is a function of the mean temperature of the cold and hot junction temperatures of the TEG modules. The electrical resistance of the TEG module decreases with an increase in the mean temperature of the cold and hot junctions of the TEG module. The mean temperature is the highest with the configuration C1 due to the higher cold junction temperature. Hence, the electrical resistance is minimal with channel configuration C1.

Fig. 13(c) shows the effect of various channel configurations on the electrical power generation by the TEG module. The total electrical power generated by the TEG modules is 4.13 W, 3.89 W, 3.95 W, 3.94 W, 3.66 W, 4.1 W, 3.73 W, 3.85 W, 4.03 W, and 3.61 W for channel configurations ranging from C1 to C10, respectively. The electric power generation by the TEG module is a function of the temperature difference between the cold and hot junction temperatures of the TEG module. The TEG electrical power generation is maximum with configurations C1 and C6 and is minimal with configuration C10.

H Electrical exergy, thermal exergy, and overall exergy of the system

Fig. 14 shows the impact of various channel configurations on the electrical exergy efficiency ($\zeta_{el}$), thermal exergy efficiency ($\zeta_{th}$), and overall exergy efficiency ($\zeta_o$) of the HCPV-T system. The $\zeta_{el}$ is 37.18 %, 37.12 %, 37.26 %, 37.28 %, 37.28 %, 37.29 %, 36.9 %, 37 %, 37.2 %, and 27 % for channel configurations ranging from C1-C10, respectively. Electrical exergy reflects the useful work derived from the system's electrical energy output. In the HCPV-T system, the total electrical energy output includes the combined power generated by the PV cell and the TEG and the frictional power losses caused by pressure drops. Since the electrical energy is entirely useable, the net electrical energy output is effectively equivalent to the total electrical exergy. $\zeta_{el}$ reaches its peak

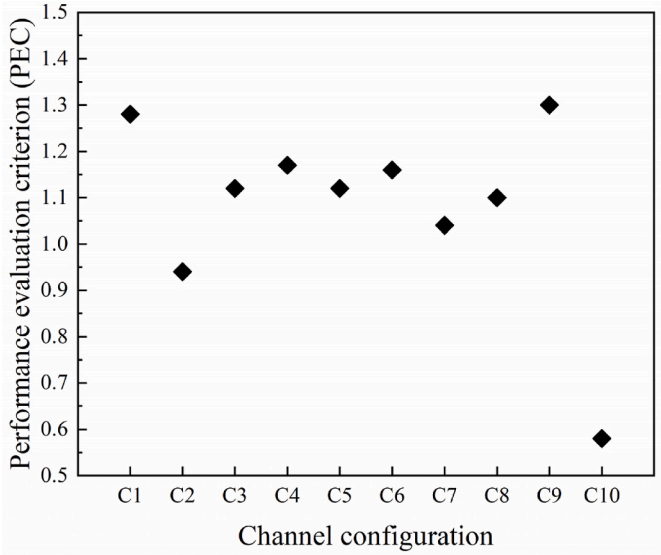



**Fig. 11.** Performance evaluation criterion for various channel configurations.

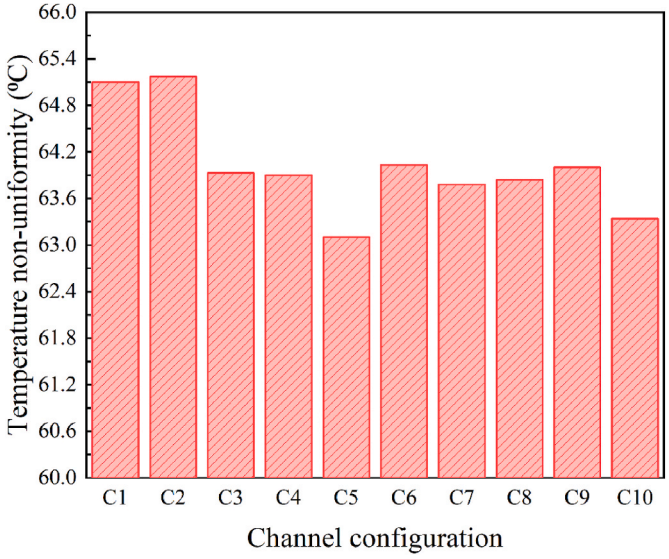



**Fig. 12.** Effect of channel configurations on temperature non-uniformity over cell surface.

with channel configuration C6 and its lowest value with channel configuration C10. The minimal electrical exergy output observed for configuration C10 is attributed to its high-pressure drop. Conversely, channel configurations C4, C5, and C6 achieve the highest electrical exergy due to a combination of efficient electrical power generation from the cell and reduced pressure drop. The $\zeta_{th}$ is 15.46 %, 15.43 %, 15.39 %, 15.36 %, 15.32 %, 15.38 %, 15.32 %, 15.33 %, 15.36 %, and 15.29 % for channel configurations ranging from C1 to C10, respectively. Thermal exergy refers to the potential of thermal energy to perform work, which is constrained by the temperature at which it is available, limiting its full conversion into useful work. The analysis reveals that $\zeta_{th}$ is highest for channel configuration C1 and lowest for channel configuration C10. A comparison of Figs. 10 and 14 further indicates that, for channel configuration C1, only 15.46 % of the total 55.4 % thermal energy output can be effectively transformed into useful work. The $\zeta_o$ is 52.64 %, 52.55 %, 52.65 %, 52.64 %, 52.61 %, 52.67 %, 52.22 %, 52.41 %, 52.59 %, and 42.34 % for channel configurations ranging from C1 to C10, respectively. The overall exergy efficiency is the combined electrical and thermal exergy efficiency of the HCPV-T system. It can be observed that the $\zeta_o$ is maximum for channel configuration C6, followed by configurations C1, C3, C4, and C5. The $\zeta_o$ indicates the total amount of work extracted from the HCPV-T system. Hence, configuration C6 provides the maximum total work output from the HCPV-T system. For comparison, the base cooling case, where no channels are introduced in the heat sink, exhibits a lower $\zeta_o$ of 49.6 %. In the literature, Abo-Zahhd et al. [5] also observed the same $\zeta_o$ of 49.2 % for the base cooling case. This demonstrates that the reported $\zeta_o$ in the current study is significantly improved over the base configurations.

I. Thermal stress ($\sigma_t$)

Fig. 15(a) shows the local thermal stress distribution along the centre line of the PV cell. It is observed from Fig. 12 that the temperature is non-uniform on the Ge cell surface. Thermal gradients are present across the surface of the Ge cell, which is connected to the top copper layer of the DBC assembly. This leads to the generation of thermal stresses. The $\sigma_t$ at the PV cell centre is 48.1 MPa, and increases to 49.37 MPa, 51.97 MPa, 55.08 MPa, 57.8 MPa, 58.45 MPa, 54.72 MPa, and 42.86 MPa at 5 mm, 10 mm, 15 mm, 20 mm, 25 mm, 30 mm, and 35 mm respectively away from the centre along the centre line. The $\sigma_t$ is minimal at the Ge cell corners and centre. The temperature at the Ge cell corners and centre is minimal due to natural convection at the corners and the CJI inlet at the centre, respectively. However, the thermal stress increases away from the centre due to higher temperature gradients. The Ge yield point is 135 MPa. Hence, the $\sigma_t$ along the centreline remains lower than the Ge yield point.

Fig. 15(b) shows the local thermal stress distribution along the diagonal line of the cell. The $\sigma_t$ at the Ge cell centre is 48.11 MPa, and increases to 50.49 MPa, 54.86 MPa, 65.26 MPa, 113.83 MPa, 130.92 MPa, 93.76 MPa, and 32.85 MPa at 5 mm, 10 mm, 15 mm, 20 mm, 25 mm, 30 mm, and 35 mm respectively away from the centre along the diagonal line of the PV cell. The $\sigma_t$ is minimal at the Ge cell centre and the extreme corners of the Ge cell due to low local temperature. However, the thermal stress increases away from the centre along the diagonal line. The thermal stress increases sharply after 20 mm along the diagonal line. The local temperature at 20 mm, 25 mm, and 30 mm away from the centre is significantly higher due to the lower thermal conductivity of the TEG module. This leads to a sharp increase in the thermal stress at these locations. However, the thermal stress at any point does not go beyond the Ge yield point.

## 7. Conclusions

This study evaluates the effect of hybrid cooling of confined jet impingement and thermoelectric generator on the HCPV-T system performance in the presence of a spectral splitter. The effect of ten channel configurations is studied by varying fin angle, fin width, and pitch. The HCPV-T system performance is observed with these channel configurations. The proposed configurations are able to achieve $T_{cell}$ in the permissible limit of 110 °C. However, the maximum cell temperature exceeds the allowable limit of 110 °C for channel configurations C1, C2, C3, C6, and C9. Hence, these channel configurations cannot be used for HCPV-T cooling. The configuration, C10, provides a minimal $T_{cell}$ of 67.47 °C. However, the pressure drop with configuration C10 is 15.4 KPa, which is significantly higher due to decreased channel width. Hence, the performance evaluation criterion for channel configuration C10 is lower. The cell average temperature and cell maximum temperature are also low for channel configurations C4, C5, and C7. However, the pressure drop is 1.4 kPa and 1.5 kPa with configurations C4 and C5, which is lower than with configuration C7. Moreover, the cell temperature non-uniformity is lower with channel configuration C5 than with configuration C7. The performance evaluation criterion (PEC) is maximum for channel configurations C4, followed by configurations C5, C8, and C6. The TEG electrical power is higher with the configuration C4

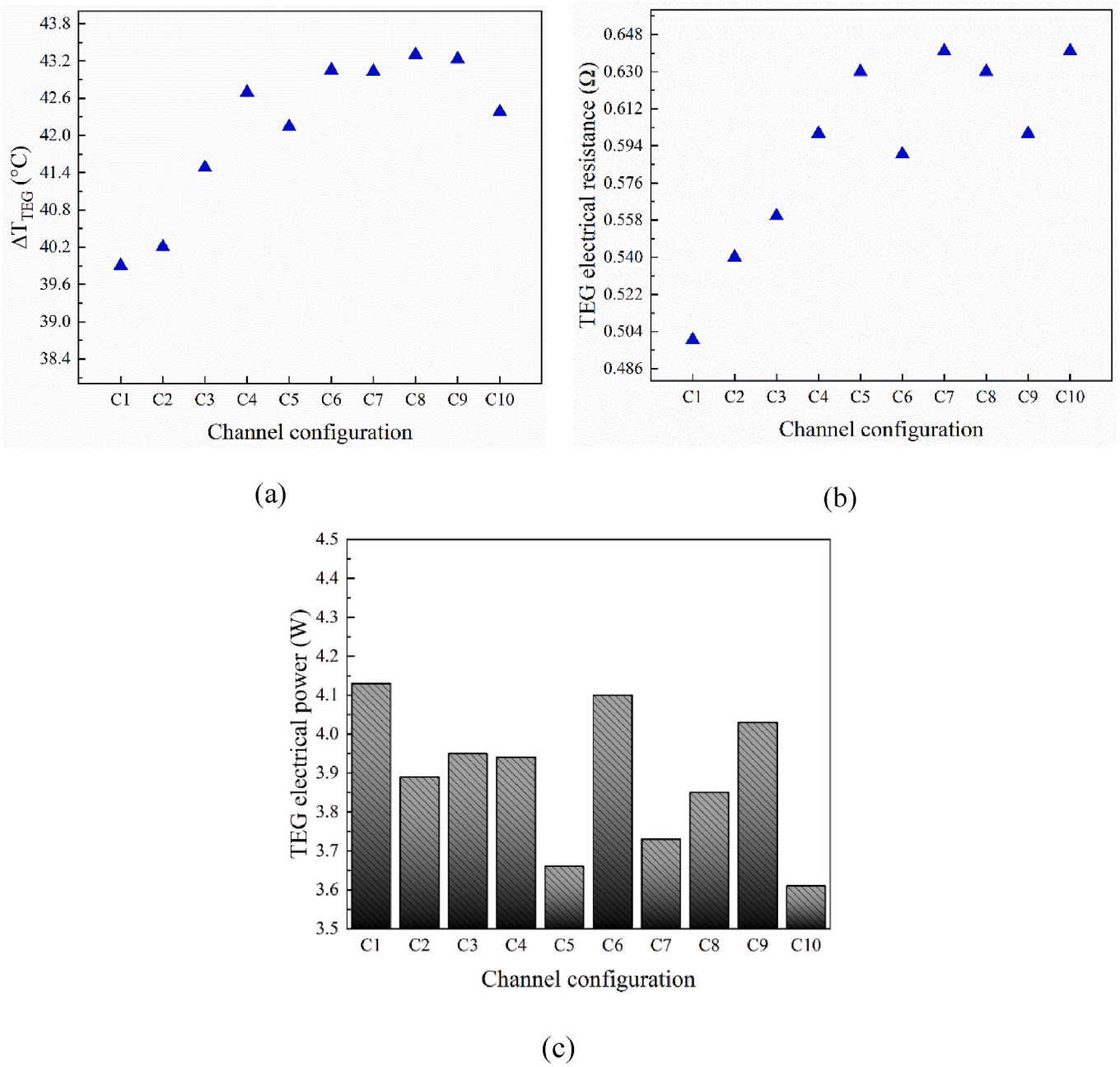



**Fig. 13.** Effect of channel configurations on (a) temperature difference between TEG junctions, (b) TEG electrical resistance, (c) power generation from TEG module.

compared to the configurations C5, C7, and C8. The overall exergy efficiency is also maximum with channel configuration C4 compared to configurations C5, C7, and C8. Hence, channel configuration C4 is the optimal configuration. The variation in thermal stress along the centre and diagonal lines of the Ge cell is also studied with configuration C5. The thermal stress is minimal at the Ge cell corners and centre, and is maximum at the TEG location. The $\sigma_t$ over the Ge cell surface is lower than the Ge yield point. The findings of this study offer valuable guidelines for future research in the design and optimization of HCPV-T systems. The configurations in the present work will be useful in the HCPV-T system thermal management with minimal pressure drop and better temperature uniformity. The comparative evaluation of ten channel configurations presents a framework for multi-parameter optimization by balancing cooling performance, electrical output, and pressure drop. The proposed hybrid cooling system can be used to generate additional electrical energy from the waste heat of the HCPV-T system by employing TEG modules, thereby improving the overall electrical efficiency of the HCPV-T system. The proposed hybrid cooling system provides an improved overall exergy efficiency of the HCPV-T system. These insights can guide future studies toward the development of advanced hybrid cooling strategies, adaptive thermal regulation techniques, and energy-harvesting enhancements for next-generation HCPV-T systems.

## CRediT authorship contribution statement

**Abhishek Gupta:** Writing – original draft, Validation, Software, Methodology, Investigation, Formal analysis, Conceptualization. **Sandesh S. Chougule:** Writing – review & editing, Supervision, Methodology, Funding acquisition, Conceptualization. **Sandip K. Saha:** Writing – review & editing, Supervision, Methodology, Funding acquisition, Conceptualization.

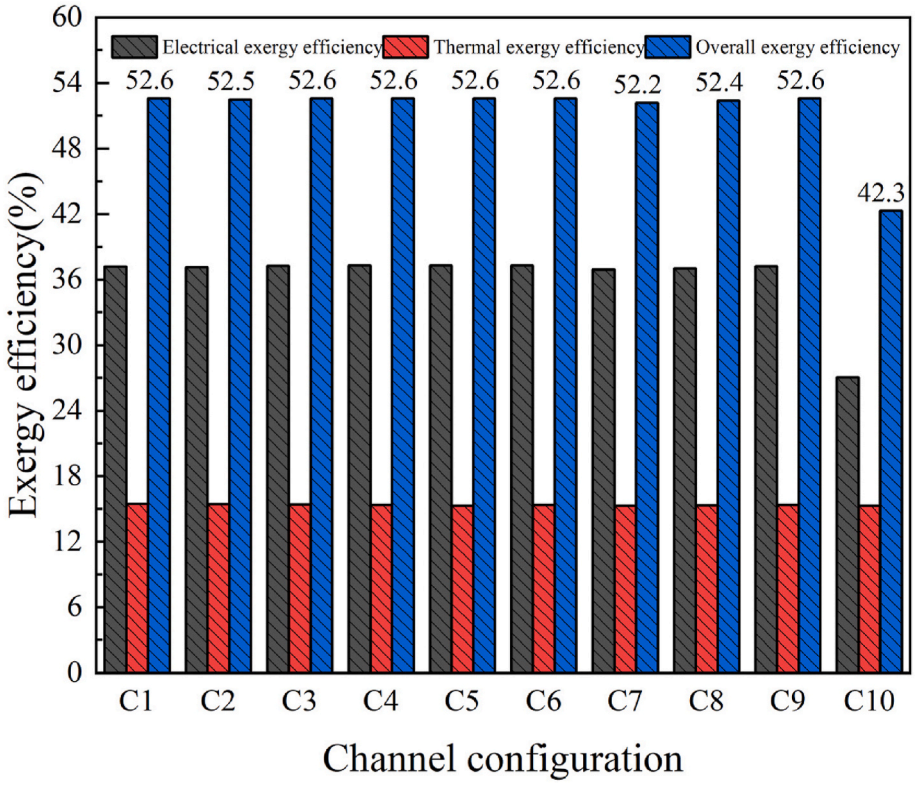



**Fig. 14.** Effect of channel configuration on electrical exergy, thermal exergy, and overall exergy of the HCPV-T system.

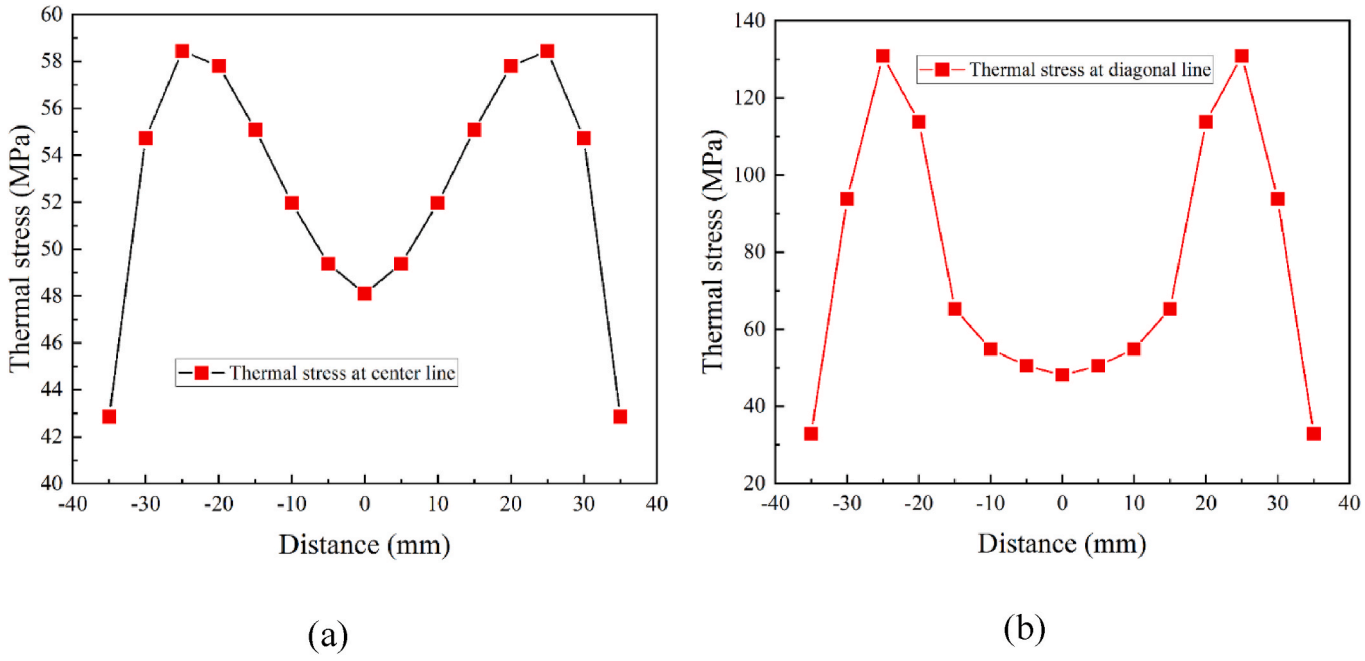



**Fig. 15.** Thermal stress variation across the Ge cell surface (a) along the centreline, (b) along the diagonal line for channel configuration C5.

## Declaration of competing interest

The authors declare the following financial interests/personal relationships which may be considered as potential competing interests: Sandesh S. Chougule reports administrative support, equipment, and supplies were provided by Imperial College London. Sandesh S. Chougule reports financial support was provided by European Commission. Sandesh S. Chougule reports financial support was provided by Science and Engineering Research Board. Abhishek Gupta reports financial support, administrative support, equipment, supplies, and writing assistance were provided by Indian Institute of Technology Bombay. If there are other authors, they declare that they have no known competing financial interests or personal relationships that could have appeared to influence the work reported in this paper.

## Acknowledgements

We wish to convey our profound gratitude to the Department of Science and Technology, India (DST) for their visionary financial support under grant number TAR/2020/000358, which was instrumental in facilitating the successful execution of this study. Our sincere thanks also extend to the European Union's Horizon 2020 Research and Innovation Program for their distinguished backing through the Marie Skłodowska-Curie Individual Fellowship, grant agreement no. 101028904-NANO-SPLIT-H2020-MSCA-IF-2020, which provided invaluable resources and opportunities for scientific advancement. Moreover, we are deeply indebted to the Horizon Europe program for their generous support through Grant Agreement ID: 101152661 under the HORIZON-TMA-MSCA-PF-EF European Fellowships. This prestigious funding enabled us to push the boundaries of our research and achieve new heights of innovation. The combined support from these esteemed institutions has been a cornerstone in the success of this endeavor, for which we are truly grateful.

## References

[1] World Energy Assessment, United Nations Development Programme, 2000.
[2] International Energy Outlook 2016 with Projections to 2040, U.S. Energy Information Administration, 2016.
[3] M. Renzi, L. Egidi, G. Comodi, Performance analysis of two 3.5 kWp CPV systems under real operating conditions, Appl. Energy 160 (2015) 687–696, https://doi.org/10.1016/j.apenergy.2015.08.096.
[4] A. Gupta, S.S. Chougule, S.K. Saha, Cooling of highly concentrated photovoltaic cells with confined jet impingement by introducing channel configurations, Renew. Energy 237 (2024) 121600, https://doi.org/10.1016/j.renene.2024.121600.
[5] E.M. Abo-Zahhad, S. Ookawara, A. Radwan, A.H. El-Shazly, M.F. ElKady, Thermal and structure analyses of high concentrator solar cell under confined jet impingement cooling, Energy Convers. Manag. 176 (2018) 39–54, https://doi.org/10.1016/j.enconman.2018.09.005.
[6] K. Nishioka, T. Takamoto, T. Agui, M. Kaneiwa, Y. Uraoka, T. Fuyuki, Annual output estimation of concentrator photovoltaic systems using high-efficiency InGaP/InGaAs/Ge triple-junction solar cells based on experimental solar cell's characteristics and field-test meteorological data, Sol. Energy Mater. Sol. Cells 90 (2006) 57–67, https://doi.org/10.1016/j.solmat.2005.01.011.
[7] S.D. Barewar, M. Joshi, P.O. Sharma, P.S. Kalos, B. Bakthavatchalam, S. S. Chougule, K. Habib, S.K. Saha, Optimization of jet impingement heat transfer: a review on advanced techniques and parameters, Therm. Sci. Eng. Prog. 39 (2023) 101697, https://doi.org/10.1016/j.tsep.2023.101697.
[8] S.S. Chougule, S.K. Sahu, Performance of carbon nanotubes-water nanofluid charged wickless heat pipe flat plate solar collectors having different filling ratio, J. Sol. Energy Eng. 137 (2015) 1–4, https://doi.org/10.1115/1.4028701.
[9] M. Modak, S. Srinivasan, K. Garg, S.S. Chougule, M.K. Agarwal, S.K. Sahu, Experimental investigation of heat transfer characteristics of the hot surface using Al2O3-water nanofluids, Chem. Eng. Process. Process Intensif. 91 (2015) 104–113, https://doi.org/10.1016/j.cep.2015.03.006.
[10] S.D. Barewar, S.S. Chougule, J. Jadhav, S. Biswas, Synthesis and thermo-physical properties of water-based novel Ag/ZnO hybrid nanofluids, J. Therm. Anal. Calorim. 134 (2018) 1493–1504, https://doi.org/10.1007/s10973-018-7883-6.
[11] P. Dwivedi, K. Sudhakar, A. Soni, E. Solomin, I. Kirpichnikova, Advanced cooling techniques of P.V. modules: a state of art, Case Stud. Therm. Eng. 21 (2020) 100674, https://doi.org/10.1016/j.csite.2020.100674.
[12] W. Li, Y. Shi, K. Chen, L. Zhu, S. Fan, A comprehensive photonic approach for solar cell cooling, ACS Photonics 4 (2017) 774–782, https://doi.org/10.1021/acsphotonics.7b00089.
[13] L. Zhu, A. Raman, K.X. Wang, M.A. Anoma, S. Fan, Radiative cooling of solar cells, Optica 1 (2014) 32, https://doi.org/10.1364/optica.1.000032.
[14] S.S. Chougule, A. Srivastava, G.G. Bolegave, B.A. Gaikwad, P.M. Shirage, C. N. Markides, Next-generation solar technologies: unlocking the potential of Ag-ZnO hybrid nanofluids for enhanced spectral-splitting photovoltaic-thermal systems, Renew. Energy 236 (2024) 121405, https://doi.org/10.1016/j.renene.2024.121405.
[15] W.H. Chen, C.C. Wang, C.I. Hung, C.C. Yang, R.C. Juang, Modeling and simulation for the design of thermal-concentrated solar thermoelectric generator, Energy (Calg.) 64 (2014) 287–297, https://doi.org/10.1016/j.energy.2013.10.073.
[16] M. Sabry, A. Lashin, M. Al Turkestani, Experimental and simulation investigations of CPV/TEG hybrid system, J. King Saud Univ. Sci. 33 (2021) 101321, https://doi.org/10.1016/j.jksus.2020.101321.
[17] H.R. Fallah Kohan, F. Lotfipour, M. Eslami, Numerical simulation of a photovoltaic thermoelectric hybrid power generation system, Sol. Energy 174 (2018) 537–548, https://doi.org/10.1016/j.solener.2018.09.046.
[18] M. Theristis, T.S. O'Donovan, Electrical-thermal analysis of III-V triple-junction solar cells under variable spectra and ambient temperatures, Sol. Energy 118 (2015) 533–546, https://doi.org/10.1016/j.solener.2015.06.003.
[19] S.D. Barewar, S. Tawri, S.S. Chougule, Heat transfer characteristics of free nanofluid impinging jet on flat surface with different jet to plate distance: an experimental investigation, Chem. Eng. Process. Process Intensif. 136 (2019) 1–10, https://doi.org/10.1016/j.cep.2018.12.001.
[20] M. Modak, S.S. Chougule, S.K. Sahu, An experimental investigation on heat transfer characteristics of hot surface by using CuO-Water nanofluids in circular jet impingement cooling, J. Heat Tran. 140 (2018) 1–10, https://doi.org/10.1115/1.4037396.
[21] A. Royne, C.J. Dey, Design of a jet impingement cooling device for densely packed PV cells under high concentration, Sol. Energy 81 (2007) 1014–1024, https://doi.org/10.1016/j.solener.2006.11.015.
[22] M. Javidan, A.J. Moghadam, Experimental investigation on thermal management of a photovoltaic module using water-jet impingement cooling, Energy Convers. Manag. 228 (2021), https://doi.org/10.1016/j.enconman.2020.113686.
[23] H.M.S. Bahaidarah, Experimental performance evaluation and modeling of jet impingement cooling for thermal management of photovoltaics, Sol. Energy 135 (2016) 605–617, https://doi.org/10.1016/j.solener.2016.06.015.
[24] S.A. Zubeer, O.M. Ali, Experimental and numerical study of low concentration and water-cooling effect on PV module performance, Case Stud. Therm. Eng. 34 (2022) 102007, https://doi.org/10.1016/j.csite.2022.102007.
[25] B. Markal, R. Varol, The Effect of Jet Impingement on the Performance of a Photovoltaic Module, 4, 2019, pp. 647–650.
[26] Y. Amanlou, T. Tavakoli Hashjin, B. Ghobadian, G. Najafi, Air cooling low concentrated photovoltaic/thermal (LCPV/T) solar collector to approach uniform temperature distribution on the PV plate, Appl. Therm. Eng. 141 (2018) 413–421, https://doi.org/10.1016/j.applthermaleng.2018.05.070.
[27] J. Dong, X. Zhuang, X. Xu, Z. Miao, B. Xu, Numerical analysis of a multi-channel active cooling system for densely packed concentrating photovoltaic cells, Energy Convers. Manag. 161 (2018) 172–181, https://doi.org/10.1016/j.enconman.2018.01.081.
[28] J. Barrau, J. Rosell, D. Chemisana, L. Tadrist, M. Ibañez, Effect of a hybrid jet impingement/micro-channel cooling device on the performance of densely packed PV cells under high concentration, Sol. Energy 85 (2011) 2655–2665, https://doi.org/10.1016/j.solener.2011.08.004.
[29] J. Tang, X. Li, R. Hu, Z. Mo, M. Du, A novel designed manifold ultrathin micro pin-fin channel for thermal management of high-concentrator photovoltaic system, Int. J. Heat Mass Tran. 183 (2022), https://doi.org/10.1016/j.ijheatmasstransfer.2021.122094.
[30] A. Shohdy, M. Emam, H. Sekiguchi, H. Hassan, Performance of new hybrid heat sink with trimmed fins and microchannels for thermal control of a triple-junction concentrator photovoltaic cell, Appl. Therm. Eng. 252 (2024), https://doi.org/10.1016/j.applthermaleng.2024.123695.
[31] J. Mohammadpour, F. Salehi, M. Sheikholeslami, A. Lee, A computational study on nanofluid impingement jets in thermal management of photovoltaic panel, Renew. Energy 189 (2022) 970–982, https://doi.org/10.1016/j.renene.2022.03.069.
[32] B. Zhao, M. Hu, X. Ao, Q. Xuan, G. Pei, Spectrally selective approaches for passive cooling of solar cells: a review, Appl. Energy 262 (2020) 114548, https://doi.org/10.1016/j.apenergy.2020.114548.
[33] A. Yusuf, S. Ballikaya, Performance analysis of concentrated photovoltaic systems using thermoelectric module with phase change material, J. Energy Storage 59 (2023), https://doi.org/10.1016/j.est.2022.106544.
[34] M.N. Shaeli, J.M. Jalil, M. Baccar, Improving the performance of solar photovoltaic thermal cells using jet impingement and phase change materials cooling technology, Renew. Energy 227 (2024) 120536, https://doi.org/10.1016/j.renene.2024.120536.
[35] F. Selimefendigil, D. Okulu, H.F. Oztop, Energy and exergy performance improvement of coupled PV–TEG module by using different shaped nano-enhanced cooling channels, Renew. Energy 234 (2024) 121059, https://doi.org/10.1016/j.renene.2024.121059.
[36] S.S. Chougule, S.K. Sahu, Thermal performance of nanofluid charged heat pipe with phase change material for electronics cooling, J. Electron. Packag. 137 (2015) 1–7, https://doi.org/10.1115/1.4028994.
[37] Z. Khalili, M. Sheikholeslami, Analyzing the effect of confined jet impingement on efficiency of photovoltaic thermal solar unit equipped with thermoelectric generator in existence of hybrid nanofluid, J. Clean. Prod. 406 (2023) 137063, https://doi.org/10.1016/j.jclepro.2023.137063.
[38] 3C44A – with 10×10 mm2Concentrator triple junction solar cell. http://www.azurspace.com, 2016, 1–6.
[39] T.G. Module, GM250-127-28-10 Thermoelectric Generator Module GM250-127-28-10 Thermoelectric Generator Generator Module, 44, 2017, pp. 1–3.
[40] L. Huaxu, W. Fuqiang, Z. Dong, C. Ziming, Z. Chuanxin, L. Bo, X. Huijin, Experimental investigation of cost-effective ZnO nanofluid based spectral splitting CPV/T system, Energy (Calg.) 194 (2020) 116913, https://doi.org/10.1016/j.energy.2020.116913.
[41] A. Aldossary, S. Mahmoud, R. Al-Dadah, Technical feasibility study of passive and active cooling for concentrator PV in harsh environment, Appl. Therm. Eng. 100 (2016) 490–500, https://doi.org/10.1016/j.applthermaleng.2016.02.023.
[42] Https://customthermoelectric.com/1261g-7l31-04cqthermoelectric-,Generator-40-x-40mm.html., Commercial TEG 1261G-7L31-04CQ data sheet, manufactured by custom thermoelectric, (n.d.).
[43] O. Hasan, A.F.M. Arif, M.U. Siddiqui, Finite element modeling, analysis, and life prediction of photovoltaic modules, J. Sol. Energy Eng. 136 (2014), https://doi.org/10.1115/1.4026037.
[44] M. Ahmed, A. Radwan, Performance evaluation of new modified low-concentrator polycrystalline silicon photovoltaic/thermal systems, Energy Convers. Manag. 149 (2017) 593–607, https://doi.org/10.1016/j.enconman.2017.07.057.
[45] S. Zimmermann, H. Helmers, M.K. Tiwari, S. Paredes, B. Michel, M. Wiesenfarth, A. W. Bett, D. Poulikakos, A high-efficiency hybrid high-concentration photovoltaic

system, Int. J. Heat Mass Tran. 89 (2015) 514–521, https://doi.org/10.1016/j.ijheatmasstransfer.2015.04.068.
[46] G. Evola, L. Marletta, Exergy and thermoeconomic optimization of a water-cooled glazed hybrid photovoltaic/thermal (PVT) collector, Sol. Energy 107 (2014) 12–25, https://doi.org/10.1016/j.solener.2014.05.041.
[47] A.G. Evans, J.W. Hutchinson, The thermomechanical integrity of thin films and multilayers, Acta Metall. Mater. 43 (1995) 2507–2530, https://doi.org/10.1016/0956-7151(94)00444-M.
[48] F. Affecting, T. Stress, C. Materials, Factors affecting thermal stress resistance, J. Am. Ceram. Soc. 61 (1953) 13.
[49] P.M. Souare, J. Sylvestre, Thermal and mechanical analysis of a concentrated photovoltaic module with integrated secondary optics, AIP Conf. Proc. 1766 (2016), https://doi.org/10.1063/1.4962114.
[50] M. Siavashi, H.R. Talesh Bahrami, E. Aminian, Optimization of heat transfer enhancement and pumping power of a heat exchanger tube using nanofluid with gradient and multi-layered porous foams, Appl. Therm. Eng. 138 (2018) 465–474, https://doi.org/10.1016/j.applthermaleng.2018.04.066.
[51] J. Lin, T. Liao, B. Lin, Performance analysis and load matching of a photovoltaic-thermoelectric hybrid system, Energy Convers. Manag. 105 (2015) 891–899, https://doi.org/10.1016/j.enconman.2015.08.054.
[52] Z. Zhang, W. Li, J. Kan, Behavior of a thermoelectric power generation device based on solar irradiation and the earth's surface-air temperature difference, Energy Convers. Manag. 97 (2015) 178–187, https://doi.org/10.1016/j.enconman.2015.03.060.
[53] A. Bitschi, Modelling of Thermoelectric Devices for Electric Power Generation, 2009, p. 144.